Precambrian Research 271 (2015) 278–294

Contents lists available at ScienceDirect

Precambrian Research

journal homepage: www.elsevier.com/locate/precamres

Newly discovered Neoproterozoic diamictite and cap carbonate (DCC) couplet in Tarim Craton, NW China: Stratigraphy, geochemistry, and paleoenvironment

Bin Wen [a,b], David A.D. Evans [b], Yong-Xiang Li [a,*], Zhengrong Wang [b,c], Chao Liu [b]

[a] State Key Laboratory for Mineral Deposits Research, School of Earth Sciences and Engineering, Nanjing University, Nanjing 210046, China
[b] Department of Geology and Geophysics, Yale University, New Haven, CT 06520-8109, USA
[c] Department of Earth and Atmospheric Sciences, City College of New York, CUNY, New York, NY 10031, USA

ARTICLE INFO

Article history:
Received 12 April 2015
Received in revised form
28 September 2015
Accepted 7 October 2015
Available online 19 October 2015

Keywords:
Diamictite-cap carbonate (DCC)
Marinoan glaciation
C isotope
Sr isotope
Mg isotope
Tarim

ABSTRACT

Neoproterozoic diamictite-cap carbonate (DCC) couplets play a pivotal role in establishing regional/interregional stratigraphic correlations and understanding the paleoenvironmental conditions following the "Snowball Earth" glaciations. Here we report newly discovered Neoproterozoic Aksu diamictite and Wushi DCC couplet from the northwestern margin of Tarim Craton, NW China. The Aksu diamictite displays glaciogenic features including striations on clasts, whereas the Wushi DCC couplet consists of discontinuous (≤1 m) matrix-supported diamictite and overlying ~1.0 to 1.7 m thick, pink dolostones. Analyses of the regional stratigraphy, sedimentological characteristics, paleontological markers, and the available radiometric ages suggest that both strata were likely related to the Marinoan glaciation and the subsequent deglaciation (ca. 635 Ma). From the cap dolostone, high-resolution $\delta^{13}C_{PDB}$ chemostratigraphy is obtained, showing almost-constant negative values (ca. −2.2 to −2.5‰), typical of Marinoan cap carbonates. In addition, the least-altered $^{87}Sr/^{86}Sr$ and $\delta^{26}Mg_{DSM3}$ records of post-glacial ocean water are extracted using a recently developed, stepwise acid-leaching method. Two groups of the least-altered $^{87}Sr/^{86}Sr$ and $\delta^{26}Mg_{DSM3}$ values are reported and can be understood under the framework of post-glacial "plumeworld". There exist slight discrepancies in $^{87}Sr/^{86}Sr$ and $\delta^{26}Mg$ between the Wushi section and sections from Australia or Mongolia, which appear to suggest different seawater environments where cap dolostones were formed.

1. Introduction

From the late Neoproterozoic to the eve of Cambrian time, Earth experienced a long tectonic transition from the dispersal of Rodinia to the subsequent amalgamation of Gondwana (e.g. Torsvik, 2003; Li et al., 2008). The transition was punctuated by multiple episodes of global-scale glaciations (e.g. Hoffman et al., 1998; Evans, 2000; Hoffman and Schrag, 2002; Hoffman and Li, 2009; Evans and Raub, 2011). Two glaciations were immediately followed by large-scale warming as indicated by the occurrence of carbonate rocks capping diamictites (e.g. Hoffman et al., 1998, 2007; Hoffman and Li, 2009; Hoffman, 2011). The characteristic diamictite-cap carbonate (DCC) couplets occurring on major cratons have been crucial for establishing regional and/or interregional stratigraphic correlations, particularly when reliable radiometric ages directly from glacial deposits are rare (e.g. Condon and Bowring, 2011), and limited fossil diversities within major eukaryotic clades before Ediacaran-Cambrian animal diversification prevent from establishing reliable biostratigraphy (Knoll et al., 2004; Knoll, 2014). The unique lithofacies and geochemical proxies of cap units including C, O, S, and Sr isotopes are potential indirect dating tools (e.g. Knoll and Walter, 1992; Kaufman and Knoll, 1995; Kaufman et al., 1997; Kennedy et al., 1998; Hoffman et al., 1998; Hoffman and Schrag, 2002; Halverson et al., 2005, 2007, 2010; Liu et al., 2013, 2014), because distinctive lithological features taken alone may be questionable (Corsetti and Kaufman, 2003). Aside from correlation purposes, the geochemistry of DCC couplets is useful for understanding the paleoenvironmental consequences of glaciations and subsequent deglaciations, including possible global-scale paleoceanographic changes associated with meltwater plumes (Shields, 2005; Hoffman, 2011; Liu et al., 2014).

Well exposed Neoproterozoic successions in Tarim Craton, northwestern China (Fig. 1), recorded multiple glaciations during the transition of supercontinent cycle (Gao and Zhu, 1984; Gao

* Corresponding author. Tel.: +86 2589680866.
E-mail address: yxli@nju.edu.cn (Y.-X. Li).

http://dx.doi.org/10.1016/j.precamres.2015.10.006
0301-9268/

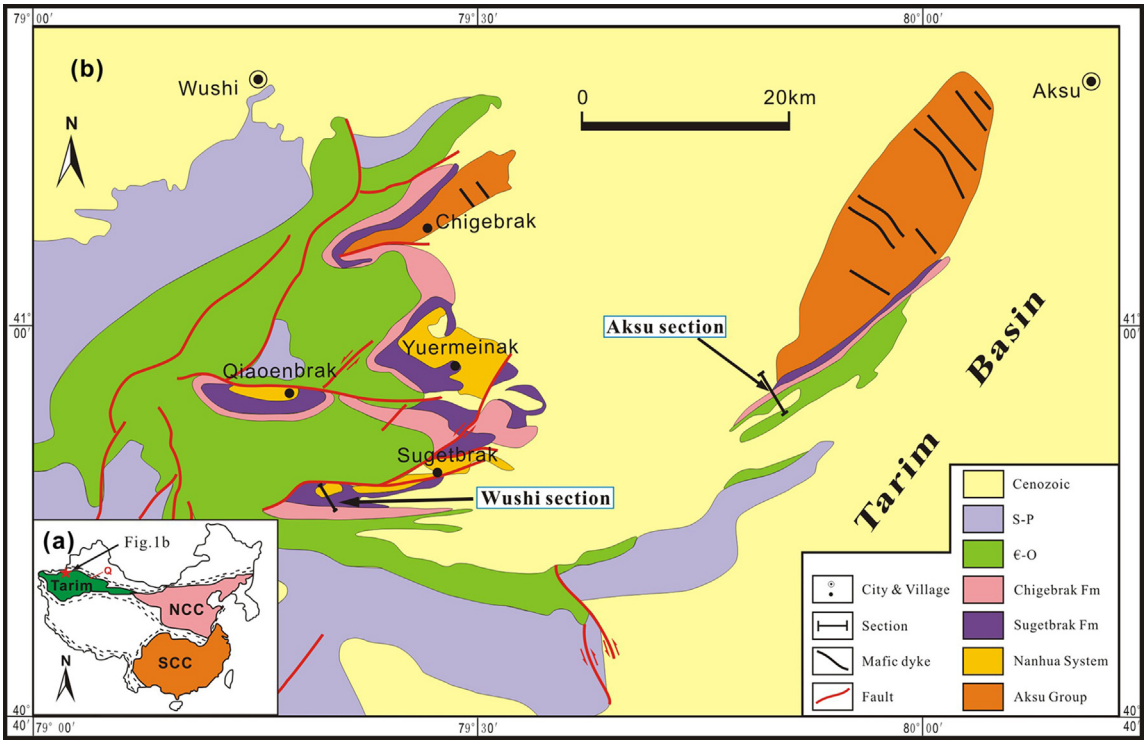

Fig. 1. (a) The major Precambrian cratons of China, showing the location of Tarim Craton (after Zhao et al., 2002). The asterisk marks the study area, which is located at the northwestern margin of the Tarim Craton, NW China. SCC, South China Craton; NCC, North China Craton; Q, Quruqtagh. (b) Geological map of the Aksu-Wushi area (modified after Gao et al., 1985; Turner, 2010). The arrows point to the two examined sections in this study.

et al., 1985; Gao and Qian, 1985; XBGMR, 1993; Xiao et al., 2004; Xu et al., 2005, 2009, 2013; Lu et al., 2008; Zhu and Wang, 2011; He et al., 2014a). However, due to the lack of suitable dating material from glacial deposits (Zhu and Wang, 2011), their ages and chronostratigraphic correlations are still ambiguous. In addition, previous studies were mainly focused on the glaciogenic successions from the Quruqtagh (also spelled as "Kuruktag" or "Kuluktage") region of eastern Tianshan (Norin, 1937; Gao and Zhu, 1984; Gao et al., 1985; Gao and Qian, 1985; XBGMR, 1993; Xu et al., 2005, 2009; Xiao et al., 2004; Shen et al., 2008; Zhu and Wang, 2011; He et al., 2014a) and relatively little attention has been paid to glacial deposits in other regions of Tarim.

Precambrian successions preserved in the Aksu-Wushi area, northwestern margin of Tarim Craton (Fig. 1), provide a key window to understand the tectonic evolution of this craton in the ancient supercontinent cycles (Chen et al., 2004; Zhan et al., 2007; Wen et al., 2013; He et al., 2014b). As one of the well-documented, Precambrian blueschists in the world, Aksu blueschists recorded a Proterozoic high pressure-low temperature metamorphism event related to oceanic subduction along the northern margin of Tarim (Liou et al., 1989, 1996; Nakajima et al., 1990; Zhu et al., 2011), and Neoproterozoic mafic dikes and lavas have been used to investigate the breakup of Rodinia (Zhang et al., 2009; Xu et al., 2013). Additionally, at least two diamictite intervals provide us a target to understand the Neoproterozoic global glaciations (Gao et al., 1985; Gao and Qian, 1985; XBGMR, 1993; Zhu and Wang, 2011). However, neither direct ages from the glacial deposits are available, nor was a complete glacial-postglacial DCC discovered previously in this area. Also, the available data are insufficient to establish their regional/interregional stratigraphic correlation, and to understand paleo-environments in the aftermath of the glaciations. For example, Ding et al. (2009) tried to obtain information about glaciations from Guozigou of the northern Tianshan region (further north of Aksu city), but the siliciclastic section there precludes stratigraphic correlation to other regions with C and O isotope results. Carbon-isotope variations have been used to correlate the succession in northwestern Tarim with that in South China (He et al., 2007; Zhan et al., 2007), but the correlation can only be made for the latest Precambrian carbonates, which are stratigraphically >400 m above the glacial deposits. Therefore, more detailed field investigations and isotope data directly from the glaciogenic successions in northwestern Tarim are needed.

In this study, we first describe the newly discovered glacial diamictites and cap carbonates in the Neoproterozoic successions from Aksu-Wushi area of the northwestern margin of Tarim Craton (Fig. 1). We then focus on chemostratigraphic analyses of the cap-carbonate unit, and discuss the paleoenvironment in the aftermath of glaciation, as well as the glacial stratigraphic framework across northern Tarim Craton during the Neoproterozoic.

2. Regional geology

Most Precambrian rocks of Tarim Craton crop out along the margins of this craton, comprising the Neoarchean to Proterozoic metamorphosed basement and the Neoproterozoic unmetamorphosed sedimentary cover (XBGMR, 1993; Lu et al., 2008; Long et al., 2010, 2012; Turner, 2010; Zhao and Guo, 2012; Zhao and Cawood, 2012; Ge et al., 2014). The Aksu-Wushi area, located at the Tarim's northwestern margin (Fig. 1), is bounded to the north by the Paleozoic Tianshan belt (Windley et al., 1990; Wang, 2006) in central Asia. In this area, the pre-Cambrian record consists of the crystalline basement of Aksu Group and the overlying unmetamorphosed sedimentary sequences (Gao et al., 1985; XBGMR, 1993; Carroll et al., 2001; Turner, 2010; Zhu et al., 2011; Xu et al., 2013). The top of the Precambrian unit is marked by a parallel unconformity right below a 5-m-thick black chert-phosphorite bed of the Cambrian limestone (Gao et al., 1985; Yao et al., 2005).

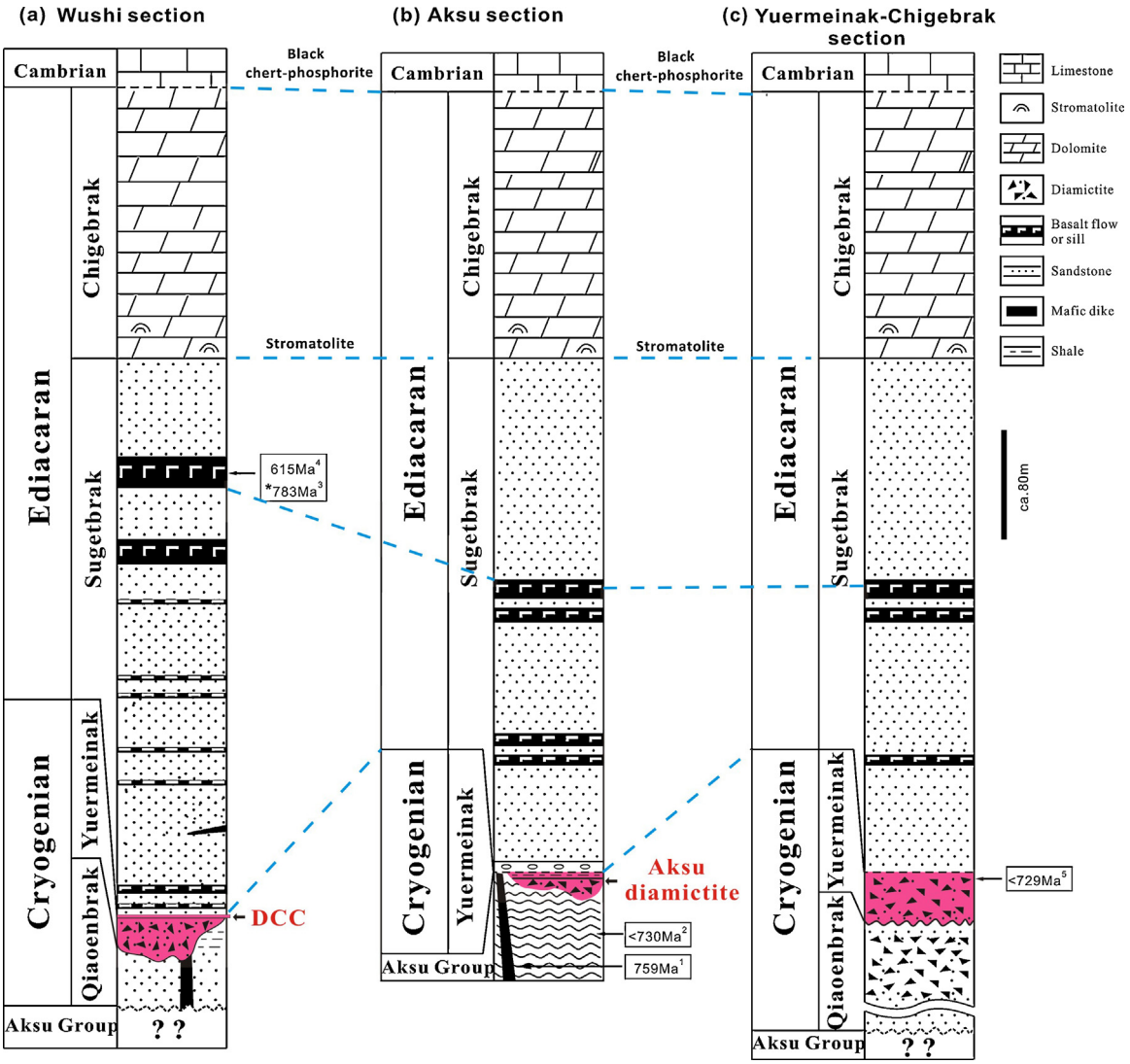

Fig. 2. The Precambrian stratigraphic framework across the whole Aksu-Wushi area of NW Tarim showing the correlations of glacial units (modified after Gao et al., 1985; XBGMR, 1993; Carroll et al., 2001; Yao et al., 2005; Turner, 2010; Zhu and Wang, 2011; see Section 3.3). Available ages are indicated (1, Zhang et al., 2009; 2, Zhu et al., 2011; 3, Zhang et al., 2012; 4, Xu et al., 2013; 5, He et al., 2014b). The age with (*) is considered as dating inherited/xenocryst zircons. DCC, diamictite and cap carbonate, same as in the following figures.

The Aksu Group is composed of pelitic, psammitic and mafic schists, and the mafic schists contain green- and blue-schists. The schists experienced multiple stages of deformation, and the blueschist facies have been interpreted to represent a Neoproterozoic subduction–accretion complex (Liou et al., 1989, 1996; Nakajima et al., 1990; Turner, 2010; Zhu et al., 2011). The basement was intruded by a series of unmetamorphosed, NW-trending mafic dikes (Liou et al., 1989, 1996; Zhang et al., 2009; Turner, 2010; Zhu et al., 2011; He et al., 2014b). Their cross-cutting relationship demonstrates that the intrusion of the mafic dikes occurred after the metamorphism of the Aksu Group, although the ages of the metamorphism of the Aksu Group and the dike intrusion are still debated (Chen et al., 2004; Zhan et al., 2007; Zhang et al., 2009; Zhu et al., 2011).

The unconformably overlying, unmetamorphosed sedimentary successions are composed of the lower Sinian Qiaoenbrak and Yuermeinak Formations, each of which contains a glacially derived unit (Gao et al., 1985; Gao and Qian, 1985; XBGMR, 1993; Zhu and Wang, 2011), and the upper Sinian Sugetbrak and Chigebrak Formations. According to the 3rd National Conference on Stratigraphy in China, the lower and upper "Sinian" were renamed as "Nanhua" and "Sinian" systems, which generally correspond to the Cryogenian and Ediacaran periods, respectively (Fig. 2; the Stratigraphy Committee of China, 2001; Gradstein et al., 2004). We adopt these new names in this paper.

In this study, we focus on two sections in this area as shown in Fig. 1b, based on our field investigations in 2011–2013. Strata in this region were gently to moderately deformed during the late Paleozoic orogenies, linked to the suturing between Tarim Craton and the more northerly terranes of the central Asian fold belt (Windley et al., 1990; Chen et al., 1999), and further warped into the broad anticlinal arches above thrust faults as a result of neotectonic intracontinental deformation within the India-Asia convergence zone (Turner et al., 2010).

3. Litho- and chrono-stratigraphy of the Aksu diamictite and Wushi DCC couplet

3.1. Aksu diamictite (Aksu section: 40.921° N, 79.831° E)

In the Aksu section, ca. 40 km southwest of Aksu city (Fig. 1b), Precambrian rocks are well exposed (the same section was described by Turner, 2010). The blueschist-bearing Aksu Group is mainly composed of metasedimentary rocks that were intruded

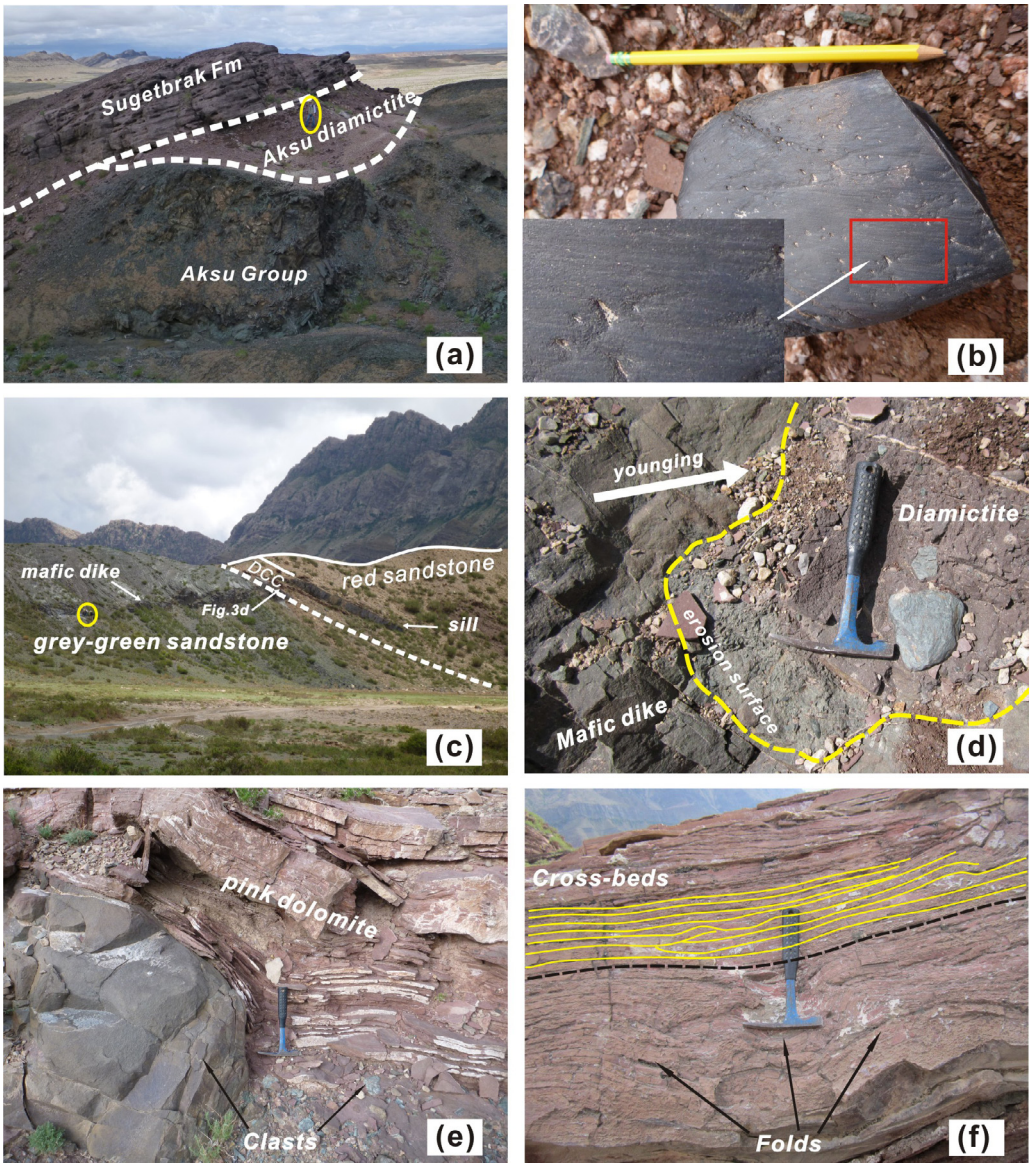

Fig. 3. Outcrop characteristics of the Aksu diamictite and the DCC couplet from the Aksu (a, b) and Wushi (c–f) sections. A person (~170 cm), a pencil (~15 cm), and a hammer (~30 cm) are for scales. (a) The Aksu diamictite unit overlies the Aksu Group with a sharp angular unconformity, and underlies the Ediacaran Sugetbrak Formation with parallel unconformity. Note the lenticularity of the exposed diamictite. (b) A striated clast eroded from the Aksu diamictite. (c) The sharp contact between the newly discovered DCC couplet and the underlying strata. The pink cap-carbonate is about 1.7 m thick. Although not readily apparent in this photograph, close inspection of the dike/DCC contact (panel d) shows that the overlying mafic sill is an unconnected, younger intrusion. (d) Oblique close-up view of the contact. The arrow approximately points to the stratigraphic younging direction. (e) Different sizes of angular to subrounded clasts within the diamictites of the DCC couplet. (f) Soft-folding structure in the lower subunit and the low-angle cross-stratification in the upper subunit of the pink dolostone of the DCC couplet.

by a series of unmetamorphosed, NW-trending mafic dikes. The mafic dikes have a SHRIMP U–Pb zircon age of 759 ± 7 Ma (Zhang et al., 2009). Unconformably overlying the Aksu Group are the Cryogenian and Ediacaran strata that show generally concordant attitudes dipping toward 160–170° at angles of 30–35°. In previous studies, the Cryogenian strata were thought to be absent, and the succession of unmetamorphosed strata commenced with basal conglomerates of the upper Ediacaran Sugetbrak Formation (Carroll et al., 2001; Turner, 2010). In our field investigations, we observed a lenticular unit that consists of shale and diamictite. This unit is separated from the underlying Aksu Group by a sharp angular unconformity, and is distinctly separated from the overlying Sugetbrak Formation by a disconformity. The exposure of this unit is not continuous and the thickness of the unit gradually decreases from 3 to 4 m at the Aksu section toward NE, and eventually the younger Ediacaran Sugetbrak Formation directly rests upon the metasedimentary basement (Fig. 3a). Farther to the northeast, clasts derived from the blueschists and mafic dikes were observed in the basal conglomerates of the Sugetbrak Formation (Liou et al., 1989, 1996; Carroll et al., 2001; Turner, 2010; Zhu et al., 2011).

The Cryogenian strata at the Aksu section contain red conglomerates and shale, previously unrecognized, in discontinuous exposures beneath the Sugetbrak Formation. The lower (<1 m) sporadically outcropped and unstratified conglomerates comprise angular to sub-rounded, poorly sorted clasts of various sizes (5–30 cm in diameter) from pebbles to cobbles. The lithologic compositions of the pebbles/cobbles are mostly the underlying blueschists and gray sandstones, and minor quartzite clasts that exhibit variably oriented striations (Fig. 3b). The variation in size and poor sorting of clasts, and especially the occurrence of striations on the clasts, indicate that the conglomerates are of glaciogenic origin (termed Aksu diamictite herein). Above the diamictite is 2–3 m thick, red shale that is interbedded with laminated green shales. The shale unit represents a lower-energy

depositional environment. A prominent ca. 5-m-thick, pebbly quartz-sandstone unit, which forms the basal conglomerate of the Sugetbrak Formation (Turner, 2010), sharply overlies the shales with concordant bedding attitudes. While the Aksu diamictite and shale are discontinuously exposed in decameter-scale paleotroughs, the basal Sugetbrak conglomerates are continuously exposed along strike for ~800 m, in many places resting directly or with an angular unconformity upon the Aksu basement schists.

The age of the Aksu diamictite is constrained by its bounding stratigraphic relationships. As a maximum age constraint, the diamictite contains clasts of the underlying blueschists, which contain detrital zircons as young as ca.730 Ma (727 ± 12 Ma; Zhu et al., 2011). However, there is inconsistency in ages, i.e., the maximum depositional age of the metasedimentary sequences is younger than the age of mafic dykes (759 ± 7 Ma; Zhang et al., 2009). If we consider analytical errors, the ages are broadly consistent; or the dated zircons from dikes are xenocrysts as proposed by Zhu et al. (2011). Either way, the depositional age of the Aksu diamictite should be younger than ~730 Ma. The minimum age of the diamictite is constrained by the overlying Sugetbrak Formation, which outcrops across the whole Aksu-Wushi area (Gao et al., 1985; XBGMR, 1993; Carroll et al., 2001; Turner, 2010).

3.2. Wushi DCC couplet (Wushi section: 40.841° N, 79.297° E)

Compared with the Aksu section, the outcrops of Cryogenian (Nanhua System) strata at Wushi section and surrounding areas are much better exposed and continuous. For instance, in the Yuermeinak and Chigebrak areas (Fig. 1b), the ≤2 km-thick Cryogenian successions which contain two diamictite levels within both the Qiaoenbrak (~100 m) and Yuermeinak Formations (~50 m) have been described in detail in previous studies (Gao et al., 1985; XBGMR, 1993; Zhu and Wang, 2011). Although the two diamictite levels occurred within sections dominated by sandstone and siltstone, the poorly sorted sub-rounded or angular clasts of various lithologies and sizes, and the occurrence of dropstones and striations on clasts (Gao and Qian, 1985; Gao et al., 1985; XBGMR, 1993; Zhu and Wang, 2011), suggest that both of them are of glacial origin. However, the top of each of the two diamictite levels is truncated by an unconformity/parallel unconformity, which hinders the glacial correlations within the Neoproterozoic time because of the uncertainties in ages of both diamictites and the missing section atop each. Although previous studies have assigned the Qiaoenbrak and Yuermeinak diamictites to Sturtian (ca. 720 Ma) and Marinoan (ca. 640 Ma) glaciations, respectively, mainly based on the relationships of depositional sequences together with limited microfossils, indirectly radiometric ages, and C-isotope excursions (as summarized by Zhu and Wang, 2011), the principal problems stated above have yet to be solved despite the fact that the maximum depositional ages of the two diamictites have been obtained recently (He et al., 2014b).

Our studied section is located more than 40 km south of Wushi and ~12 km west of the Sugetbrak area (Fig. 1b), where the Cryogenian strata are exposed around a broad "dome" structure in an area of ~5 km^2. Here we report, for the first time in this area, the discovery of a distinct diamictite and cap carbonate (DCC) couplet at the base of the Sugetbrak Formation (Fig. 3c). With an angular unconformity below this DCC unit, the Cryogenian strata comprise rhythmic beds of dominantly gray-green and minor red-colored grit, arkose, greywacke, siltstone, and mudstone, all moderately west-dipping. A series of mafic dikes penetrated into the succession (Fig. 3c). The dikes are parallel to each other with NW strikes, and are not more than 1 m in width.

Both the sedimentary rocks and the dikes are truncated by an erosional unconformity, blanketed by the DCC unit that gently dips outward around the "dome" (Fig. 1b). This newly recognized DCC couplet contains a pink or red, matrix-supported diamictite unit, and an overlying pink to rose-colored dolostone. The diamictite unit is laterally discontinuous around the western dome margin, nowhere exceeding ~1 m thickness. The diamictite contains angular to sub-rounded, gray-green shale and sandstone clasts, ranging from pebble to boulder size and derived from the underlying gray-green colored succession, "floating" within a red-brown sandstone or siltstone matrix (Fig. 3d and e). The cap dolostone, directly covering the diamictite or gritty sandstone, is ~1.0–1.7 m thick and consists of thin-laminated micritic dolostone. It can be further subdivided into two subunits according to different sedimentary features. The lower subunit is about 30–50 cm thick and displays abundant soft-folding structures (Fig. 3f), and sometimes shows bedding-parallel sheet-crack cements which occurred in other cap dolostones as well (Hoffman, 2011). In the westward section, the lower dolostone beds are represented by draping structures wrapping some breccias; while to the east of a smaller scale, the lower subunit begins with ca.10 cm thick hematitic shaly beds. In contrast to these features, the upper subunit exhibits relatively planar and parallel laminations with some low-angle cross-stratifications (Fig. 3f). Such features suggest that the lower subunit was precipitated in a high-energy environment while the upper subunit was deposited in a relatively quiescent environment. The lower subunit probably recorded an abrupt sea level rise outpacing the regional effects of isostatic unloading during transition from icehouse to greenhouse (Hoffman and Schrag, 2002; Nogueira et al., 2003). The DCC couplet is conformably overlain by the ~1000 m thick Sugetbrak Formation (Fig. 2a), beginning with a ~10 m thick red shale or siltstone unit and continuing upward with decameter/hectometer-thick intervals of massive to cross-bedded red sandstone, yellowish siltstone, and basalt.

3.3. Regional stratigraphic framework and glacial correlations

The new discoveries of the Aksu diamictite and the Wushi DCC couplet from this study can help establish the Precambrian stratigraphic framework in the Aksu-Wushi area of NW Tarim. As described above, both the Aksu diamictite and the Wushi DCC couplet act as the bridging strata from Cryogenian (Nanhua System) to Ediacaran (Sinian) periods in this region, namely, the cap carbonate unit of the Wushi DCC fills the gap between the underlying diamictite and the overlying Sugetbrak Formation which has caused the stratigraphic ambiguities in this area for a long time (Gao et al., 1985; XBGMR, 1993; Zhu and Wang, 2011; Xu et al., 2013; He et al., 2014b). With this in mind, we will establish the stratigraphic framework from a broad perspective.

From the regional perspective, the Aksu diamictite, Wushi DCC couplet and Yuermeinak diamictite (the Yuermeinak-Chigebrak area) are all overlain by the Ediacaran Sugetbrak Formation (Fig. 2; Gao et al., 1985; XBGMR, 1993; Zhu and Wang, 2011), and the Sugetbrak Formation can be considered as an essential marker for the stratigraphic correlations. Meanwhile, the stratigraphic correlations of the Sugetbrak Formation and the conformably overlying Chigebrak Formation across the whole Aksu-Wushi area have been well documented in previous studies (e.g. Gao et al., 1985; XBGMR, 1993; Carroll et al., 2001; Turner, 2010) based on the key stratigraphic and paleontological markers, including the non-marine to marine sedimentary transition between the two formations (Gao et al., 1985; Liou et al., 1989, 1996; XBGMR, 1993; Turner, 2010), stromatolites at the base of the Chigebrak Formation (Gao et al., 1985; XBGMR, 1993; Carroll et al., 2001; Turner, 2010) and the acritarch assemblages and small shelly fossils from the Early Cambrian black chert-phosphorite layer (Yao et al., 2005). On the other hand, the Wushi DCC couplet represents a unique glaciation-deglaciation succession in the Cryogenian/Ediacaran period. Our field investigations together with previous studies (Gao et al., 1985;

XBGMR, 1993; Carroll et al., 2001; Turner, 2010; Xu et al., 2013; He et al., 2014b) did not recognize an additional glacial unit, nor sedimentary hiatus/tectonic activity, between the boundary of the Wushi DCC/Sugetbrak Formation and the Cambrian black chert-phosphorite in the whole Aksu-Wushi area. Also, there are reasons to believe that both the Aksu and Yuermeinak diamictites are most likely the equivalents of the Wushi DCC (Fig. 2). First, the three diamictite units share the similar stratigraphic positions, i.e., all are below the Sugetbrak Formation; Second, all three units display similar sedimentological characteristics of red color (this study; Gao et al., 1985; Gao and Qian, 1985; XBGMR, 1993; Zhu and Wang, 2011), which may imply that they were deposited in a similar paleoenvironment; Third, the age of Aksu diamictite (ca. <730 Ma) is consistent with the maximum depositional age of the Yuermeinak diamictite (729 ± 7 Ma; He et al., 2014b); Fourth, all the three diamictite units are separated from the underlying strata by an unconformity, which may indicate that they were probably formed after the same widespread tectonism in the NW Tarim.

Based on the above analyses, a regional stratigraphic framework across the whole Aksu-Wushi area of NW Tarim has been established (Fig. 2). In the correlations, the age of the glaciation, i.e., the Aksu-Yuermeinak diamictite and Wushi DCC is constrained by their bounding strata. As described above, the glaciation should be younger than ca. 730 Ma. Also, the overlying Sugetbrak Formation can provide a minimum age constraint (Fig. 2). Recently, two U–Pb zircon ages of ca. 783 Ma and ca. 615 Ma (Zhang et al., 2012; Xu et al., 2013) have been obtained from the basalt layers near the top of the Sugetbrak Formation. The ca. 783 Ma age is older than the maximum depositional age of the metasedimentary Aksu Group (ca. 730 Ma; Zhu et al., 2011) and the Yuermeinak Formation (ca. 729 Ma; He et al., 2014b), probably representing an inherited age of zircons. The ca. 615 Ma age is consistent with the maximum depositional age of the (upper) Sugetbrak Formation of ca. 620–600 Ma (Zhu et al., 2011; He et al., 2014b). Therefore, the ca. 615 Ma age likely represents the true crystallization age of the basaltic flows. Thus, the glaciation age is constrained within the interval of ca. 730–615 Ma, which is compatible with the age of the late Cryogenian Marinoan glaciation that was dated at ca. 640 Ma in South China (Condon et al., 2005; Zhang et al., 2008) and at similar ages elsewhere in the world (Hoffmann et al., 2004; Calver et al., 2013).

In addition, the sedimentary characteristics and depositional environment of the cap dolostones in Wushi are similar to those of well-known Marinoan-age cap carbonates in the world. The cap dolostones in the Wushi DCC show distinct pinkish color and low-angle cross-beddings, which are very similar to the type post-Marinoan cap dolostones (e.g. Hoffman and Schrag, 2002; Raub, 2008; Hoffman, 2011), although the Wushi section lacks the tube stones and trochoidal structures commonly found in other sections (Hoffman and Schrag, 2002; Corsetti and Grotzinger, 2005; Allen and Hoffman, 2005; Macdonald et al., 2009; Rose and Maloof, 2010); Also, the occurrence of a large amount of hematite within the cap dolostones of the Wushi DCC (Wen, 2014) suggests that it may be formed in an oxic environment, which is similar to the contemporaneous cap carbonates from Brazil (Font et al., 2005) and southern Australia (Raub et al., 2007; Raub, 2008). In summary, the Wushi DCC is likely of Marinoan age (~635 Ma).

4. Chemostratigraphy

4.1. Methods

Samples for geochemical analyses were collected from the cap unit of the DCC couplet at the Wushi section (Figs. 2 and 4). Cylindrical cores were drilled every ~5 cm using a portable gasoline-powered drill from the ~1.7 m thick cap dolostone. In the laboratory, samples were first cut to expose fresh surfaces, then were crushed and ground into ≤100 mesh powder in an agate mortar. For samples with carbonate cement veins, sample powder was collected using a microdrill to avoid macroscopic veins. Altogether, 28 samples were analyzed for carbon- and oxygen-isotope compositions; 8 representative samples were measured for $^{87}Sr/^{86}Sr$ ratios, as well as trace metal concentrations, among which 5 samples were also analyzed for Mg isotope compositions. All geochemical analyses were carried out at Yale University.

Approximately 200 μg powder of each sample was reacted with ultra-high-purity phosphoric acid (UHPP acid with a concentration >105%) for more than 12 h to liberate CO_2 for the analysis of carbon and oxygen isotope compositions following Wang et al. (2013a) in the Earth System Center for Stable Isotopic Studies (ESCSIS) at Yale University. Two aliquots of each sample were measured with one aliquot reacting at 25 °C and the other at 75 °C, in an attempt to identify the C–O isotope compositions of calcite and dolostone components in samples. Results of $\delta^{13}C$ and $\delta^{18}O$ are reported in delta notation as per mil (‰) relative to Vienna Pee Dee Belemnite (VPDB) standard. Repeated measurements of an in-house standard (SECM) show typical precision of ~0.09‰ and ~0.09‰ (1σ, $n = 5$) for $\delta^{13}C$ and $\delta^{18}O$, respectively, for analysis conducted at 25 °C, and of ~0.2‰ and ~0.1‰ (1σ, $n = 5$), respectively, for analysis conducted at 75 °C.

Eight representative samples (AK6-4-2, AK6-4-10A, AK6-4-11, AK6-4-13, AK6-4-18, AK6-4-19, AK6-4-23 and AK6-4-26) were analyzed for Sr, Mg isotope compositions and element concentrations using an incremental leaching technique (Liu et al., 2013, 2014). It has been demonstrated that this method can effectively extract geochemical signatures of various phases including the surface adsorbed phase, calcite, dolomite, and clay minerals (Liu et al., 2013, 2014; Liu, 2014). In practice, about 200 mg powder from each sample was weighed and loaded into a pre-cleaned centrifuge tube, and then leached at 20 °C following a 15-step leaching procedure: N1–N2, 5 mL 1 M ammonium acetate; S1–S7, 5 mL 0.25 vol.% acetic acid; S8–S10, 6 mL 1 vol.% acetic acid; S11–S12, 3 mL 5 vol.% acetic acid and S13, 6 mL 10 vol.% acetic acid (Liu et al., 2013, 2014). At each step, sample tubes were ultrasonically agitated for 10 min, and were then centrifuged at 3600 rpm for 5 min; supernatants were collected for isotopic and elemental analysis, while the residues in the centrifuge tubes were used for further leaching. In order to assess what minerals and how much had been dissolved during the stepwise leaching, elements (Mg, Ca, Mn, Sr, Rb and Ba) in all leachates for each sample were measured before the ion-exchange column experiments for Sr and Mg purified. For samples with large portions of secondary calcite indicated by lower Mg/Ca (<0.6; Fig. 6c) and more radiogenic $^{87}Sr/^{86}Sr$ values (details in the below), step S13 was repeated three more steps (S14–S16) in order to identify the most primitive dolomite component. A second aliquot of leachates, from all steps of four samples (AK6-4-2, AK6-4-10a, AK6-4-19 and AK6-4-23) and last four steps (S10–S13) of four samples (AK6-4-11, AK6-4-13, AK6-4-18 and AK6-4-26), was analyzed for $^{87}Sr/^{86}Sr$, and leachates from the most primitive dolomite in five samples were analyzed for Mg isotope composition. All elemental and isotopic analyses were conducted using single-collector ICP-MS (Element-XR) and MC-ICP-MS (Neptune), respectively.

Extractions of pure Sr and Mg by ion-exchange columns were performed in the geochemical clean lab at Yale University following the procedures established by Liu et al. (2013, 2014) and Wang et al. (2013b), after which pure Sr and Mg were dissolved in 5 wt% HNO_3 (ρ=1.020 g/ml) for isotopic analysis using MC-ICP-MS (Neptune). For the Sr isotope analysis, standard samples NBS 987 ($^{87}Sr/^{86}Sr = 0.71025$) and modern seawater/coral ($^{87}Sr/^{86}Sr = 0.709175$) were processed through ion exchange columns along with sample solutions, and were used for mass-bias corrections. During the Mg isotope measurement, the technique of sample-standard bracketing was applied: i.e.,

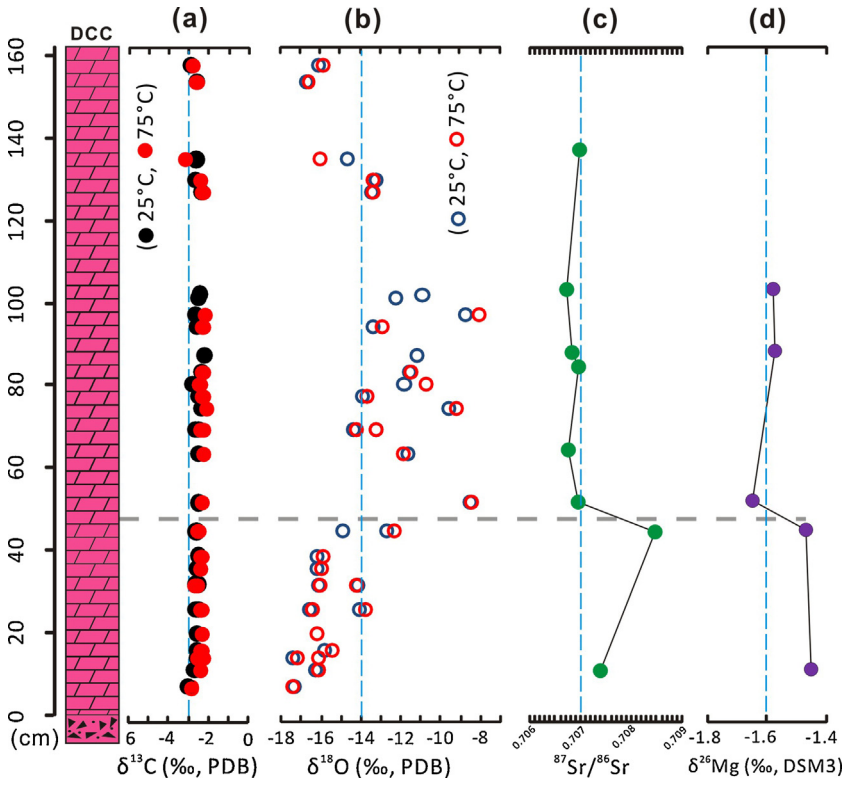

Fig. 4. Chemostratigraphic ($\delta^{13}C$, $\delta^{18}O$, $^{87}Sr/^{86}Sr$ and $\delta^{26}Mg$) profiles of the overlying dolostone of the DCC couplet from the Wushi section. The gray dashed line marks the boundary between the lower and upper subunits of the dolostones according to the characteristics of sedimentary facies and isotopic profiles.

every two samples were bracketed by two or three standards with known $\delta^{26}Mg$ (‰) values calibrated against DSM3 (Wang et al., 2013b; Saenger and Wang, 2014). All Mg isotope compositions in this paper were expressed as $\delta^{26}Mg$ (‰) calculated by $(R^{26/24}_{sample}/R^{26/24}_{DSM3} - 1) \times 100$, where is the $^{26}Mg/^{24}Mg$ ratio of DSM3 standard (Galy et al., 2003).

To better understand the stratigraphic and glacial correlations between the Aksu-Wushi area and the typical Quruqtagh area of eastern Tianshan of NE Tarim, we analyzed additional $^{87}Sr/^{86}Sr$ data of the Tereeken cap dolostone (i.e., the Zhamoketi Formation) from the Quruqtagh Yukkengol section (Fig. 7a of Xiao et al., 2004). Previously published $^{87}Sr/^{86}Sr$ results of these samples range from 0.71195 to 0.71364 (Xiao et al., 2004), which are more radiogenic than those of the contemporaneous seawater/glacial meltwater plume (Halverson et al., 2007, 2010; Liu et al., 2013, 2014). The $\delta^{13}C$ and $\delta^{18}O$ data of these samples have been published by Xiao et al. (2004) and Shen et al. (2008).

4.2. Results

4.2.1. Dolostones of the Wushi DCC

(1) *Carbon and oxygen isotopes.* The high-resolution $\delta^{13}C$ and $\delta^{18}O$ data are listed in Table 1, and the isotopic profiles through cap dolostone of the DCC couplet are shown in Fig. 4a and b. The $\delta^{13}C$ values of dolostone measured at 75 °C are systematically higher than those measured at 25 °C by up to 0.3‰ (Fig. 5a). The $\delta^{18}O$ values of dolostone measured at 75 °C are also systematically higher than those measured at 25 °C by up to 0.7‰ (Fig. 5b). Moreover, in both cases, there are no statistically significant correlations between $\delta^{18}O$ and $\delta^{13}C$ values of dolostone when $\delta^{18}O_{PDB}$ >−16‰ (Fig. 5c).

In the chemo-stratigraphic profiles ($\delta^{13}C$, $\delta^{18}O$, $^{87}Sr/^{86}Sr$ and $\delta^{26}Mg$), $\delta^{13}C$ values obtained at 25 °C and 75 °C are around −2.5‰ and −2.2 to −2.4‰ (Table 1 and Fig. 4a). The $\delta^{18}O$ profile begins with extremely low values of ca. −17‰ at the bottom, increases to ca. −8‰ in the middle, and ends with values of −14 to −16‰ at the top (Table 1 and Fig. 4b). Overall, the $\delta^{18}O$ values define a different trajectory relative to $\delta^{13}C$, i.e., $\delta^{18}O$ values are more negative and scattered than $\delta^{13}C$.

(2) *Dissolution of cap carbonates.* The elemental (Mg, Ca, Mn, Sr, Rb and Ba) concentrations together with X-ray diffraction (XRD) data of samples can provide a better understanding of the mineralogy of the rocks. They contain >35% CaO, <10% or ~10% MgO in the lower (below ~0.45 m) and upper subunits of the cap carbonates (Fig. 4), respectively, corresponding to calcareous dolostones. Except the ammonium acetate washing in the first two steps, the weight percentage (wt.%) of dissolved carbonates in each step are shown in Table 2 and Fig. 6a. All the samples present a similar trend of carbonates soluble in the weak acetic acid (0.25 vol%) from step 3 to 9, carbonates released in the acid in each step is ~4 to 6%. But in the following steps, the amounts of carbonates dissolved in each step are varying from sample to sample (Fig. 6a), suggesting the heterogeneity in samples. For samples AK6-4-2 and AK6-4-10a, the maximum amounts (>10%) of dissolutions occur in steps 10 and 11, while for samples AK6-4-19 and AK6-4-23, they occur in step 16. In addition, carbonates in the former samples have been almost completely leached out by step 15, while the leaching for the latter samples lasts until step 18 (Fig. 6a). Nevertheless, in any case, a cumulative 70–80% or more of total carbonates are dissolved from each sample at the end of the leaching experiments, and the data of isotopes and elements can be used for further discussion.

(3) *Results of Sr and Mg isotopes and trace-element ratios.* $^{87}Sr/^{86}Sr$ and elemental molar ratios in all leaching steps for the four representative samples (AK6-4-2, AK6-4-10a, AK6-4-19 and AK6-4-23) are summarized in Table 2 and plotted in Fig. 6. Except for the sample AK6-4-10a that shows unsystematic fluctuations (Fig. 6b), the $^{87}Sr/^{86}Sr$ ratios for each of other samples decrease continuously

Table 1
Carbon and oxygen isotope data from the cap dolostones of the Wushi DCC.

Sample	Height (cm)	Lithology	$\delta^{13}C_{PDB}$ (‰, 25 °C)	$\delta^{13}C_{PDB}$ (‰, 75 °C)	$\delta^{13}O_{PDB}$ (‰, 25 °C)	$\delta^{13}O_{PDB}$ (‰, 75 °C)
AK6-4-1	7	Dolostone	−3.0	−2.8	−17.3	−17.5
AK6-4-2	11	Dolostone	−2.6	−2.3	−16.3	−16.1
AK6-4-3A	14	Dolostone	−2.5	−2.2	−17.4	−17.2
AK6-4-3B	14	Dolostone		−2.5		−16.2
AK6-4-4	16	Dolostone	−2.5	−2.3	−15.8	−15.4
AK6-4-5	20	Dolostone	−2.5	−2.2		−16.2
AK6-4-6A	26	Dolostone	−2.4	−2.3	−16.5	−16.5
AK6-4-6B	26	Dolostone	−2.5	−2.3	−14.0	−13.7
AK6-4-7A	32	Dolostone	−2.4	−2.6	−16.1	−16.0
AK6-4-7B	32	Dolostone	−2.6	−2.5	−14.1	−14.2
AK6-4-8	36	Dolostone	−2.5	−2.3	−16.1	−16.0
AK6-4-9	39	Dolostone	−2.4	−2.3	−16.1	−15.9
AK6-4-10A	45	Dolostone	−2.5		−14.9	
AK6-4-10B	45	Dolostone	−2.5	−2.4	−12.7	−12.3
AK6-4-11	52	Dolostone	−2.4	−2.3	−8.5	−8.4
AK6-4-12	56	Dolostone				
AK6-4-13	64	Dolostone	−2.4	−2.2	−11.6	−11.9
AK6-4-14A	70	Dolostone	−2.5	−2.2	−14.3	−14.2
AK6-4-14B	70	Dolostone	−2.4	−2.4	−13.2	−13.2
AK6-4-15	75	Dolostone	−2.3	−2.1	−9.5	−9.2
AK6-4-16	78	Dolostone	−2.4	−2.2	−13.9	−13.7
AK6-4-17	81	Dolostone	−2.7	−2.4	−11.8	−10.7
AK6-4-18	84	Dolostone	−2.3	−2.2	−11.5	−11.5
AK6-4-19	88	Dolostone	−2.1		−11.2	
AK6-4-20	95	Dolostone	−2.5	−2.2	−13.3	−12.9
AK6-4-21	98	Dolostone	−2.6	−2.1	−8.7	−8.0
AK6-4-22	102	Dolostone	−2.4		−12.2	
AK6-4-23	103	Dolostone	−2.4		−10.9	
AK6-4-24	128	Dolostone	−2.3	−2.2	−13.5	−13.4
AK6-4-25	131	Dolostone	−2.6	−2.4	−13.2	−13.4
AK6-4-26	136	Dolostone	−2.5	−3.1	−14.7	−16.1
AK6-4-27	155	Dolostone	−2.5	−2.5	−16.7	−16.6
AK6-4-28	159	Dolostone	−2.8	−2.7	−16.1	−15.9

with the progress of incremental leaching, reaching the lowest values in step S12 or S14 where a large portion of sample (cumulative 70% or more; Table 2) has been dissolved, and then rise in the last few steps (Table 2 and Fig. 6b). In all samples, Mg/Ca ratios start from low values (less than 0.2) in the first few steps, and increase gradually to a constant value of 0.7–1.0 in the last 3–6 steps (Fig. 6c). The Sr/Ca and Rb/Sr ratios show a similar trend before step S10: both decrease rapidly from a high value and then reach a plateau, but Sr/Ca remains at a plateau value afterwards (Fig. 6d) while Rb/Sr returns to a higher value (Fig. 6e). Mn/Sr ratios increase to the highest values first, and then show a steady decline although the decreasing rates are different for different samples (Fig. 6f).

The minimum $^{87}Sr/^{86}Sr$ with the corresponding $\delta^{26}Mg_{DSM3}$ (‰) and elemental ratio values from each sample are summarized in Table 3. The $^{87}Sr/^{86}Sr$ ratios are corrected for ^{87}Rb-decay using the age of ca. 635 Ma (varying the age by 100 Ma will result into changes typically shown in the 5th or 6th decimal points). The stratigraphic profiles of the $^{87}Sr/^{86}Sr$ and $\delta^{26}Mg_{DSM3}$ are plotted in Fig. 4c and d, along with the $\delta^{13}C$ and $\delta^{18}O$ data in the section. The $^{87}Sr/^{86}Sr$ and $\delta^{26}Mg$ profiles exhibit similar patterns throughout the cap-dolostone unit of the DCC couplet. $^{87}Sr/^{86}Sr$ ratios begin with a slightly high value of 0.70739 at the bottom of the section, rise to 0.70843 at the height of ~0.45 m, and then decrease to roughly-constant values around 0.70700 at the height of ~0.52 m (Fig. 4c), whilst the $\delta^{26}Mg$ profile decreases from −1.41 to −1.45‰ to a low-value plateau of −1.57 to −1.65‰ (Table 3 and Fig. 4d). It is interesting that the height (ca. 0.5 m) of the transitions is coincident with the sedimentological boundary described in Section 3.2. The elemental ratios (Mg/Ca, Sr/Ca, Mn/Sr and Rb/Sr) corresponding to the minimum $^{87}Sr/^{86}Sr$ ratios in all samples are also listed in Table 3. In all samples, Mg/Ca ratios are roughly constant around ca. 0.8–0.9 mol/mol (except one <0.7), Sr/Ca ratios are in the range of 124–180 μmol/mol (corresponding to 50–100 ppm Sr within samples), Mn/Sr ratios are between 7 and 14 mol/mol, Rb/Srratios are in the range of 2.4–15.3 mmol/mol.

4.2.2. Cap dolostone in the Zhamoketi Formation (Quruqtagh)

The $^{87}Sr/^{86}Sr$ and elemental ratios of all leaching supernatants for the selected cap-dolostone samples (Delta 11, 15, 39 and 57) in the Zhamoketi Formation are listed in Tables 2 and 3, and plotted in Fig. 7. Unlike the samples from Wushi DCC, these cap dolostones exhibit highly consistent variations of $^{87}Sr/^{86}Sr$, elemental ratios and amounts of carbonates dissolved with the leaching steps (Fig. 7). In all four samples, $^{87}Sr/^{86}Sr$ ratios of supernatants stay at a plateau with high values between ca. 0.711 and 0.713 before step S13, after which they continuously decrease until reaching their lowest values in step S17, and then sharply increase in the last step (Table 2 and Fig. 7a). Mg/Ca ratios show very low values (<0.2 mol/mol) in the first 3–5 steps and then increase gradually, reaching a constant value of 0.7–1.0 before the decrease in the last step (Fig. 7c). The Sr/Ca ratios keep decreasing with continued leaching (Fig. 7d). The Rb/Sr ratios reach the lowest values after the first couple steps leached by 1 M ammonium, and then increase slowly before the rapid rise in the last step (Fig. 7e). Mn/Sr ratios display two stages of steady increase and decrease before and after the step S14 (Fig. 7f). Compared with the cap dolostone of Wushi DCC, the minimum strontium values in samples of the Zhamoketi Formation show a slighter variation from 0.70760 to 0.70880 (Rb-decay corrected; Table 3).

5. Discussion

5.1. Cap dolostone of the Wushi DCC

5.1.1. Least-altered strontium and magnesium isotopes

The $^{87}Sr/^{86}Sr$ variations in different leaching steps of each sample (Fig. 6b) can be attributed to multiple Sr sources including

Table 2
Weight percentage (wt.%), $^{87}Sr/^{86}Sr$, and elemental ratios in all leaching steps of representative samples from the Wushi DCC and Quruqtagh cap carbonates. Notes: Stars mark the least-altered values for each sample. The number in the parentheses is the 1σ; analytical error in the last digit. Same as in the following tables.

Area	Step	$^{87}Sr/^{86}Sr$	Mg/Ca (mol/mol)	Sr/Ca (μmol/mol)	Mn/Sr (mol/mol)	Rb/Sr (mmol/mol)	Leachate carbonate/ sample (wt.%)	Step	$^{87}Sr/^{86}Sr$	Mg/Ca (mol/mol)	Sr/Ca (μmol/mol)	Mn/Sr (mol/mol)	Rb/Sr (mmol/mol)	Leachate carbonate/ sample (wt.%)
Wushi		AK6-4-2							AK6-4-10A					
	N1	0.71116(18)	0.01(1)	535(21)	4(1)	2.1(2)		N1	0.70922(12)	0.09(1)	359(15)	3(1)	21.0(2)	
	N2	0.71120(10)	0.01(1)	391(16)	9(1)	0.5(1)		N2	0.70875(17)	0.07(1)	272(11)	7(1)	9.1(1)	
	S1	0.71115(8)	0.01(1)	368(15)	6(1)	0.1(1)	5.4	S1	0.70844(10)	0.02(1)	268(11)	6(1)	3.3(1)	5.5
	S2	0.71108(13)	0.01(1)	372(15)	8(1)	0.2(1)	4.9	S2	0.70865(12)	0.02(1)	247(10)	8(1)	1.8(1)	5.3
	S3	0.71109(9)	0.01(1)	358(15)	10(1)	0.3(1)	5.4	S3	0.70940(61)	0.02(1)	248(10)	13(1)	1.0(1)	4.6
	S4	0.71113(11)	0.01(1)	375(16)	9(1)	0.2(1)	5.3	S4	0.70843(14)	0.01(1)	259(11)	12(1)	0.7(1)	5.5
	S5	0.71114(8)	0.01(1)	387(16)	10(1)	0.3(1)	5.3	S5	0.70841(14)	0.01(1)	252(9)	14(1)	0.5(1)	1.3
	S6	0.71113(9)	0.01(1)	376(16)	11(1)	0.2(1)	4.6	S6	0.70855(10)	0.01(1)	245(10)	16(1)	0.5(1)	4.6
	S7	0.71106(8)	0.01(1)	387(16)	11(1)	0.2(1)	3.7	S7	0.70847(11)	0.01(1)	254(10)	15(1)	0.5(1)	2.6
	S8	0.71094(10)	0.07(1)	349(15)	12(1)	0.2(1)	13.0	S8	0.70829(19)	0.14(1)	226(10)	17(1)	0.6(1)	16.5
	S9	0.71080(13)	0.09(1)	338(15)	12(1)	0.3(1)	12.8	S9	0.70814(11)	0.34(1)	196(8)	17(1)	2.4(1)	7.4
	S10	0.71002(9)	0.44(1)	243(9)	15(1)	1.5(1)	2.6	*S10	0.70872(13)	0.63(2)	155(6)	14(1)	11.3(1)	1.9
	S11	0.70850(15)	0.76(4)	160(11)	15(2)	10.3(2)	0.9	S11	0.70995(24)	0.89(5)	160(13)	12(2)	42.7(11)	0.8
	*S12	0.70778(21)	0.83(7)	149(18)	12(3)	15.3(6)	0.6	S12	0.70855(22)	1.03(16)	168(38)	15(6)	47.3(23)	0.3
	S13	0.70800(34)	0.79(21)	194(60)	10(7)	18.7(19)	0.2	S13	0.71141(32)	0.86(28)	197(76)	16(10)	82.0(56)	0.2
		AK6-4-19							AK6-4-23					
	N1	0.70922(10)	0.03(1)	314(12)	9(1)	5.7(1)		N1	0.70889(14)	0.03(1)	240(9)	12(1)	5.4(1)	
	N2	0.70864(18)	0.01(1)	229(9)	19(1)	1.0(1)		N2	0.70844(9)	0.01(1)	216(8)	18(1)	2.6(1)	
	S1	0.70836(10)	0.01(1)	214(9)	14(1)	0.6(1)	5.0	S1	0.70832(8)	0.01(1)	204(8)	13(1)	1.4(1)	4.6
	S2	0.70825(14)	0.01(1)	212(9)	17(1)	1.0(1)	5.3	S2	0.70823(8)	0.01(1)	202(8)	17(1)	0.8(1)	4.2
	S3	0.70793(20)	0.01(1)	204(8)	21(1)	1.1(1)	5.5	S3	0.70806(8)	0.04(1)	199(8)	26(1)	0.6(1)	3.9
	S4	0.70772(18)	–	–	–	0.8(1)		S4	0.70793(6)	0.06(1)	200(8)	23(1)	0.9(1)	4.5
	S5	0.70793(5)	0.17(1)	184(7)	22(1)	1.1(1)	4.1	S5	0.70770(7)	0.21(1)	188(7)	23(1)	1.4(1)	2.6
	S6	0.70783(6)	0.26(1)	187(7)	19(1)	2.0(1)	2.9	S6	0.70781(6)	0.15(1)	186(7)	25(1)	1.3(1)	3.2
	S7	0.70782(6)	0.33(1)	187(7)	19(1)	1.4(1)	2.2	S7	0.70766(7)	0.26(1)	207(8)	21(1)	1.9(1)	2.3
	S8	0.70768(5)	0.39(1)	187(7)	17(1)	2.0(1)	4.4	S8	0.70762(6)	0.28(1)	197(8)	19(1)	2.1(1)	3.5
	S9	0.70760(6)	0.46(2)	184(7)	16(1)	2.1(1)	2.7	S9	0.70739(6)	0.40(1)	197(8)	17(1)	1.1(1)	4.4
	S10	0.70771(5)	0.32(1)	185(8)	17(1)	1.1(1)	8.2	S10	0.70736(6)	0.51(1)	191(7)	16(1)	1.5(1)	3.1
	S11	0.70744(5)	0.52(2)	171(6)	13(1)	6.6(1)	3.9	S11	0.70710(6)	0.63(2)	193(7)	14(1)	1.8(1)	3.8
	S12	0.70744(5)	0.55(2)	171(7)	14(1)	4.9(1)	4.2	S12	0.70706(6)	0.55(2)	188(7)	12(1)	3.2(1)	3.5
	S13	0.70736(6)	0.62(2)	171(7)	14(1)	8.3(1)	4.7	S13	0.70698(6)	0.69(2)	184(7)	11(1)	5.4(1)	4.2
	*S14	0.70687(4)	0.88(3)	132(11)	7(1)	2.4(1)	12.1	*S14	0.70680(3)	0.91(3)	180(15)	7(1)	2.9(1)	11.7
	S15	0.70699(10)	0.86(3)	122(11)	8(1)	7.0(1)	2.1	S15	0.70692(7)	0.87(3)	194(15)	6(1)	6.0(1)	1.8
	S16	0.70740(16)	0.88(4)	120(22)	7(3)	14.1(2)	1.0	S16	0.70691(7)	0.86(3)	165(15)	7(1)	7.0(1)	1.6
Quruqtagh		Delta 11							Delta 15					
	N1	0.71289(2)	0.07(1)	1956(174)	3(1)	2.5(1)		N1	0.71250(2)	0.09(1)	1918(166)	3(1)	4.1(2)	
	N2	0.71297(4)	0.02(1)	1649(145)	6(1)	0.7(1)		N2	0.71263(2)	0.04(1)	1652(144)	7(1)	1.1(1)	
	S1	0.71302(2)	0.02(1)	1646(148)	7(1)	0.1(1)	5.8	S1	0.71259(2)	0.02(1)	1427(128)	14(1)	0.1(1)	4.8
	S2	0.71274(2)	0.01(1)	1620(146)	7(1)	0.1(1)	5.4	S2	0.71202(2)	0.02(1)	1455(131)	11(1)	0.1(1)	5.4
	S3	0.71258(2)	0.01(1)	1640(148)	8(1)	0.1(1)	5.6	S3	0.71199(2)	0.10(1)	1272(114)	16(1)	0.2(1)	4.6
	S4	0.71254(2)	0.12(1)	1426(128)	11(1)	0.2(1)	4.2	S4	0.71216(2)	0.38(1)	974(86)	18(2)	0.5(1)	3.7
	S5	0.71257(3)	0.31(1)	1143(101)	13(1)	0.2(1)	3.7	S5	0.71211(3)	0.34(1)	1004(89)	17(2)	0.4(1)	3.3
	S6	0.71253(2)	0.31(1)	1113(98)	13(1)	0.2(1)	3.3	S6	0.71219(3)	0.50(2)	814(71)	20(2)	0.5(1)	2.7
	S7	0.71254(3)	0.36(1)	1028(90)	14(1)	0.5(1)	3.3	S7	0.71206(3)	0.53(2)	807(68)	20(2)	0.5(1)	1.9
	S8	0.71256(3)	0.39(1)	1008(90)	15(1)	0.2(1)	6.2	S8	0.71202(3)	0.37(1)	928(82)	19(2)	0.3(1)	3.9
	S9	0.71239(2)	0.39(1)	952(85)	16(1)	0.2(1)	6.6	S9	0.71188(2)	0.51(2)	699(61)	22(2)	0.5(1)	3.7
	S10	0.71233(3)	0.67(2)	523(45)	29(3)	0.8(1)	4.8	S10	0.71170(3)	0.50(3)	726(64)	22(2)	0.6(1)	4.9
	S11	0.71214(2)	0.76(3)	434(37)	34(3)	0.8(1)	4.3	S11	0.71182(3)	0.69(2)	524(45)	28(2)	0.7(1)	3.6
	S12	0.71182(4)	0.81(3)	297(24)	48(4)	0.6(1)	3.7	S12	0.71169(6)	0.79(3)	379(31)	35(3)	0.9(1)	3.4
	S13	0.71158(4)	0.85(3)	252(21)	56(5)	1.5(1)	4.7	S13	0.71156(4)	0.86(3)	312(26)	37(3)	1.2(1)	5.3
	S14	0.71027(6)	0.68(3)	179(11)	51(4)	11.5(5)	0.9	S14	0.71014(4)	0.88(3)	230(12)	40(2)	8.4(2)	1.9
	S15	0.70933(9)	0.73(5)	148(15)	49(5)	11.5(8)	0.7	S15	0.70886(5)	0.72(3)	174(9)	33(2)	7.4(2)	1.6

S16	0.70866(9)	0.77(5)	120(17)	40(7)	18.3(18)	0.6	S16	0.70808(6)	0.79(3)	147(9)	32(2)	7.9(4)	1.1	
*S17	0.70831(14)	0.68(7)	110(26)	25(9)	28.1(50)	0.4	*S17	0.70787(17)	0.87(4)	147(12)	24(3)	11.3(7)	0.9	
S18	0.71594(491)	0.26(20)	79(95)	3.9(37)	282.8(500)	0.1	S18	0.70935(38)	0.51(17)	124(60)	5(15)	93.1(417)	0.2	
	Delta 39							Delta 57						
N1	0.71271(3)	0.17(1)	1771(156)	7(1)	4.7(2)		N1	0.71279(4)	0.16(1)	1693(149)	5(1)	4.6(2)		
N2	0.71246(3)	0.07(1)	1989(199)	10(1)	0.9(1)		N2	0.71309(4)	0.07(1)	1706(150)	7(1)	1.2(1)		
S1	0.71181(4)	0.06(1)	1969(177)	15(1)	0.1(1)	3.8	S1	0.71278(5)	0.12(1)	1481(133)	15(1)	0.2(1)	4.0	
S2	0.71168(5)	0.31(1)	1376(123)	23(2)	0.3(1)	3.6	S2	0.71311(4)	0.48(1)	1003(88)	24(2)	0.6(1)	3.3	
S3	0.71195(5)	0.40(1)	1223(108)	24(2)	0.3(1)	3.2	S3	0.71310(5)	0.58(2)	827(71)	29(3)	1.0(1)	2.8	
S4	0.71219(6)	0.57(2)	986(86)	28(2)	0.5(1)	2.7	S4	0.71341(4)	0.70(2)	727(62)	33(3)	0.7(1)	2.6	
S5	0.71240(6)	0.65(2)	845(71)	30(3)	0.5(1)	1.9	S5	0.71323(5)	0.70(2)	711(60)	35(3)	0.6(1)	2.3	
S6	0.71245(5)	0.63(2)	863(72)	30(3)	0.5(1)	1.6	S6	0.71330(5)	0.70(2)	652(54)	34(3)	0.5(1)	2.0	
S7	0.71251(6)	0.72(2)	707(58)	34(3)	0.9(1)	1.7	S7	0.71336(3)	0.75(2)	616(50)	37(3)	0.7(1)	1.7	
S8	0.71233(5)	0.66(2)	817(71)	31(3)	0.6(1)	3.4	S8	0.71311(2)	0.65(2)	753(65)	30(3)	0.6(1)	3.1	
S9	0.71275(6)	0.74(2)	545(47)	40(4)	1.3(1)	4.1	S9	0.71327(3)	0.82(3)	511(42)	41(4)	0.9(1)	2.5	
S10	0.71257(9)	0.81(3)	456(38)	44(4)	0.9(1)	3.3	S10	0.71310(3)	0.84(3)	449(37)	44(4)	1.1(1)	3.0	
S11	0.71241(9)	0.81(3)	417(36)	45(4)	0.8(1)	4.6	S11	0.71309(3)	0.84(3)	395(33)	44(4)	1.3(1)	3.1	
S12	0.71284(9)	0.76(3)	388(33)	48(4)	0.8(1)	4.8	S12	0.71342(3)	0.84(3)	421(36)	49(4)	0.4(1)	5.0	
S13	0.71230(9)	0.82(3)	325(28)	54(5)	2.6(1)	6.9	S13	0.71269(3)	0.85(3)	333(29)	55(5)	1.3(1)	6.6	
S14	0.71152(9)	0.83(3)	280(16)	60(4)	5.1(1)	2.7	S14	0.71151(3)	0.85(3)	269(15)	66(4)	6.7(2)	2.5	
S15	0.71030(9)	0.91(4)	228(12)	56(4)	4.7(1)	2.5	S15	0.71039(4)	0.96(4)	238(13)	55(3)	7.4(2)	2.0	
S16	0.70936(9)	0.79(3)	166(10)	35(3)	8.3(4)	1.0	S16	0.70955(5)	0.80(3)	182(95)	48(3)	6.6(2)	1.5	
*S17	0.70865(10)	0.76(6)	179(20)	20(4)	15.2(13)	0.5	*S17	0.70898(7)	0.92(4)	191(12)	39(3)	8.2(4)	0.9	
S18	0.70950(20)	0.57(16)	153(56)	9(11)	48.9(128)	0.2	S18	0.71295(69)	0.30(28)	182(114)	1(18)	100.0(670)	0.1	

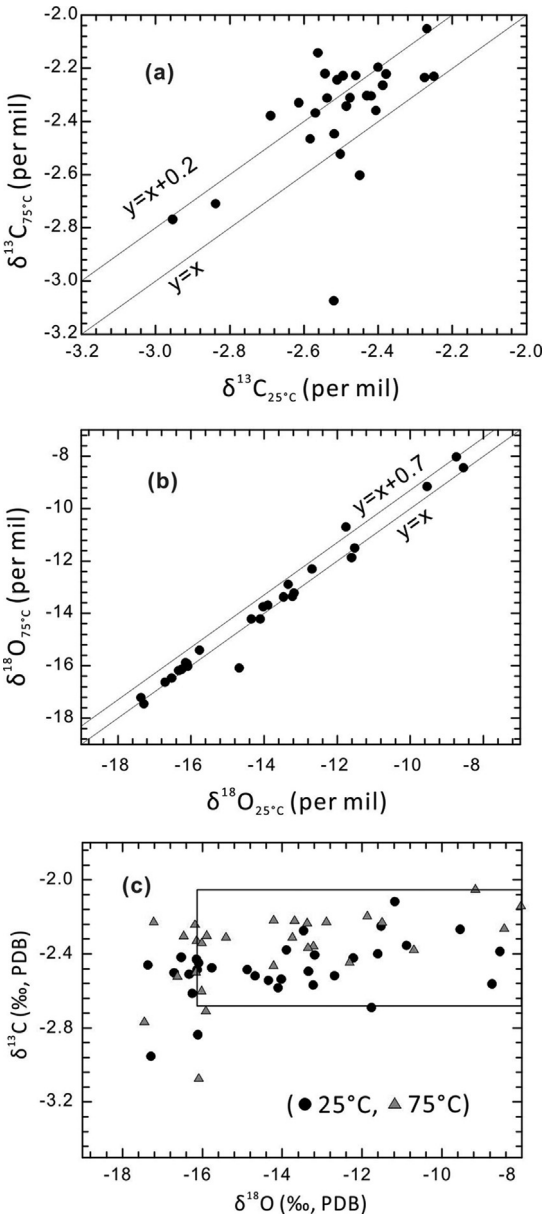

Fig. 5. Results of carbon and oxygen isotope compositions from cap dolostone of the Wushi DCC couplet. (a) Comparison of $\delta^{13}C_{PDB}$ values measured at 25 °C and 75 °C; (b) comparison of $\delta^{18}O_{PDB}$ values measured at 25 °C and 75 °C; (c) the relationships between $\delta^{18}O_{PDB}$ and $\delta^{13}C_{PDB}$ values of dolostone measured at 25 °C and 75 °C.

surface adsorbates, evaporated salts, secondary calcites, dolomites, and clay minerals (Gao, 1990; Bailey et al., 2000; Liu et al., 2013, 2014). Specifically, the first two leaching steps (N1–N2) mainly leached out the surface adsorbed ions or evaporated salts (Bailey et al., 2000; Liu et al., 2013), indicated by their significantly radiogenic $^{87}Sr/^{86}Sr$, and high Sr/Ca and Rb/Sr ratios (Fig. 6b, d and e). In the following steps, the radiogenic Sr, Sr/Ca and Rb/Sr ratios continue to decrease, while Mg/Ca ratios start to increase (Fig. 6c). These results suggest that secondary calcite is leached in earlier steps, followed by dissolution of dolomite in later steps. The trend of rapid-increase in the Mn/Sr ratio, before reaching the highest values (Fig. 6f), reflects that a large amount of Mn is dissolved from the secondary calcite. Until the step yielding the minimum $^{87}Sr/^{86}Sr$ values, $^{87}Sr/^{86}Sr$ and Mn/Sr ratios of supernatants continue to decrease, Mg/Ca ratios stay within 0.7–0.9, Sr/Ca ratios reach a lower plateau value, while Rb/Sr ratios slightly increase,

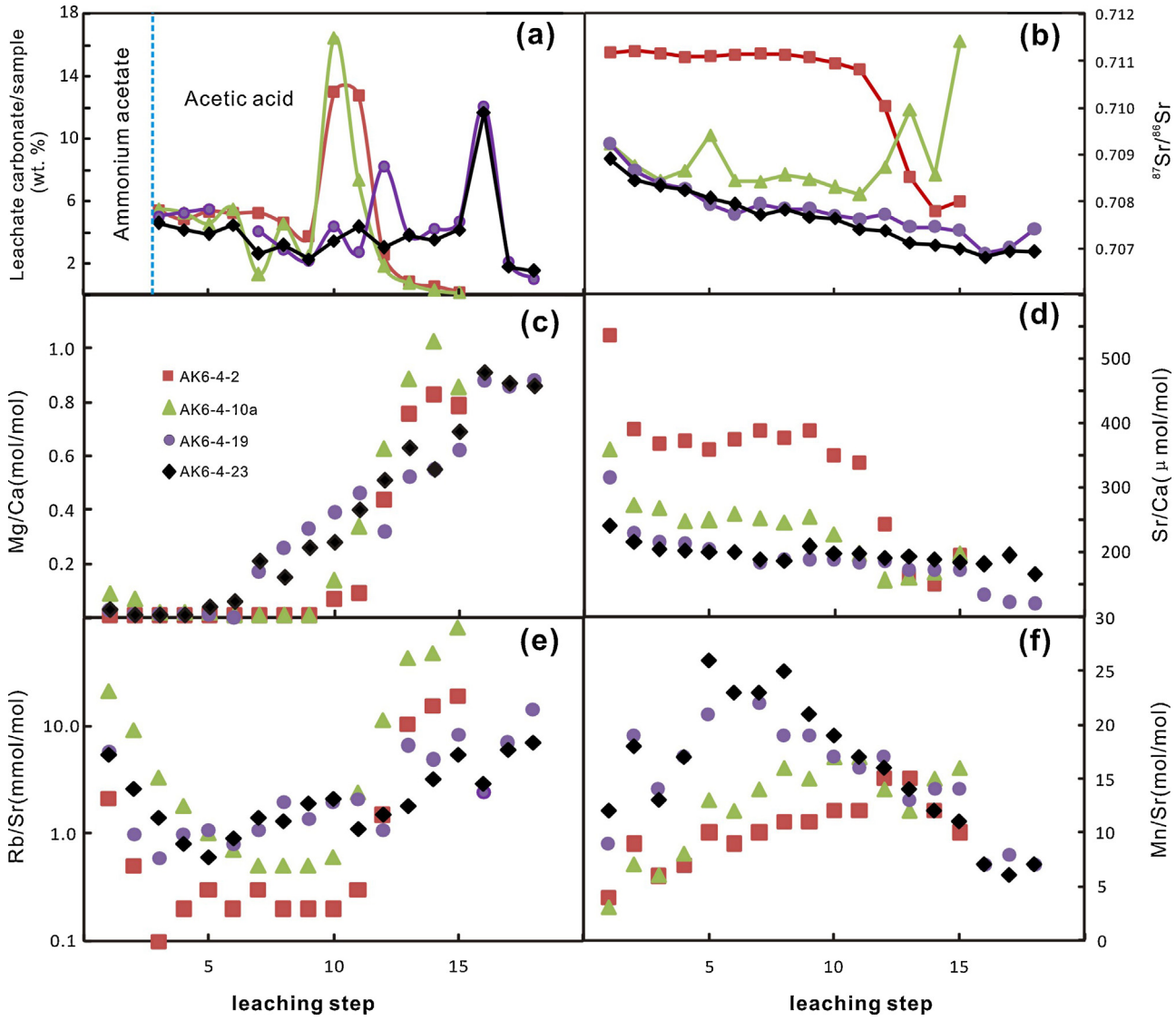

Fig. 6. Variations in weight percentage (wt.%), $^{87}Sr/^{86}Sr$, and elemental ratios with leaching steps (four representative samples from cap dolostone of Wushi DCC are shown). The lowest $^{87}Sr/^{86}Sr$ value from each sample could define the value with the minimum contamination.

suggesting that the dolomite is dominantly dissolved by the acid. After the leaching step where the minimum $^{87}Sr/^{86}Sr$ is reached, $^{87}Sr/^{86}Sr$ and Rb/Sr ratios increase rapidly, indicating that more radiogenic Sr is contributed from non-carbonates, such as the clay minerals (Bailey et al., 2000; Liu et al., 2013, 2014). In this context, the Sr sources and elements are sequentially contributed from secondary calcites, dolomites and clay minerals in samples during the step-leaching experiments, and the minimum $^{87}Sr/^{86}Sr$ value corresponds to the least-altered dolomite phase in each sample. In addition, very low values of Mn/Sr and Rb/Sr ratios correspond to the minimum $^{87}Sr/^{86}Sr$ values (Table 3). Therefore, we interpret the Sr and Mg isotopes corresponding to the least-altered dolomite in

Table 3
Isotopes and elemental ratios from the steps with minimum $^{87}Sr/^{86}Sr$ values in each sample of the cap dolostones from the Wushi DCC and Quruqtagh.

Area	Sample	Height (m)	$^{87}Sr/^{86}Sr$	$^{87}Sr/^{86}Sr$ (Rb-decay corrected)	Mg/Ca (mol/mol)	$\delta^{26}Mg_{DSM3}$ (‰)	Sr/Ca (μmol/mol)	Mn/Sr (mol/mol)	Rb/Sr (mmol/mol)
Wushi	AK6-4-2	0.11	0.70778 (21)	0.70739 (26)	0.83 (2)	−1.45 (3)	149(18)	12(3)	15.3(6)
	AK6-4-10A	0.45	0.70872(13)	0.70843 (13)	0.63 (2)	−1.41 (2)	155(6)	14(1)	11.3(1)
	AK6-4-11	0.52	0.70707 (6)	0.70696 (6)	0.88 (4)	−1.65 (2)	124(8)	12(1)	4.6(1)
	AK6-4-13	0.64	0.70687 (3)	0.70676 (3)	0.84 (3)	–	155(11)	8(1)	4.4(1)
	AK6-4-18	0.84	0.70711 (4)	0.70697 (4)	0.82 (3)	–	146(10)	11(1)	5.4(2)
	AK6-4-19	0.88	0.70687 (4)	0.70681 (4)	0.88 (3)	−1.57 (1)	132(11)	7(1)	2.4(1)
	AK6-4-23	1.03	0.70680 (3)	0.70672 (3)	0.91 (3)	−1.58 (3)	180(15)	7(1)	2.9(1)
	AK6-4-26	1.36	0.70713 (6)	0.70699 (6)	0.79 (3)	–	160(12)	10(1)	5.8(1)
Quruqtagh	Delta 11	0.03	0.70831 (14)	0.70760 (19)	0.68 (7)	–	110(26)	25(9)	28.1(50)
	Delta 15	0.18	0.70787 (17)	0.70760 (7)	0.87 (4)	–	147(12)	24(3)	11.3(7)
	Delta 39	2.54	0.70865 (10)	0.70830 (10)	0.76 (6)	–	179(20)	20(4)	15.2(13)
	Delta 57	5.97	0.70898 (7)	0.70880 (7)	0.92 (4)	–	191(12)	39(3)	8.2(4)

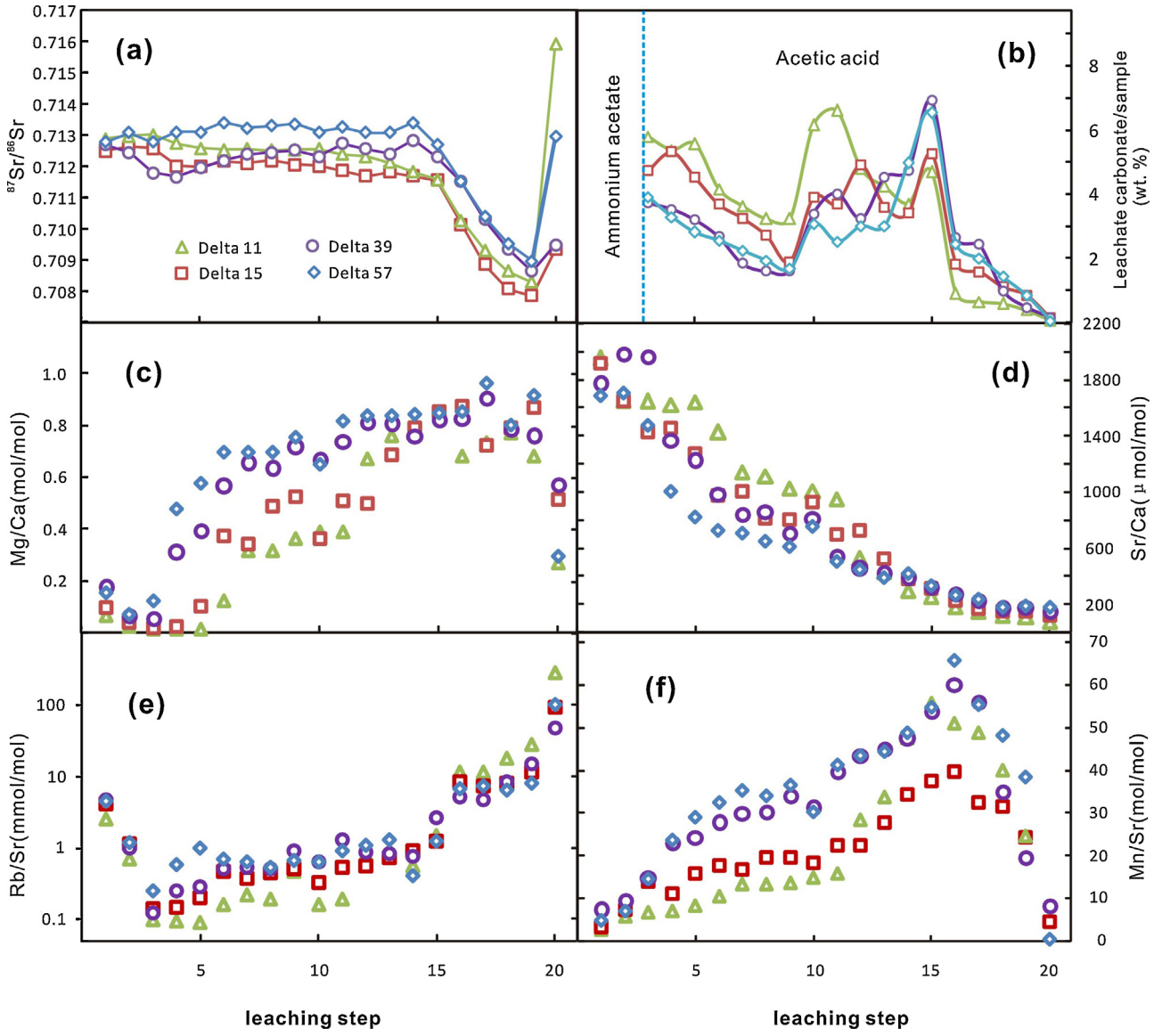

Fig. 7. Variations in weight percentage (wt.%), $^{87}Sr/^{86}Sr$, and elemental ratios with leaching steps of the selected samples from Zhamoketi Formation (cap dolostone of the Tereeken glaciation) in Quruqtagh area of eastern Tianshan (NE Tarim). The lowest $^{87}Sr/^{86}Sr$ value for each sample could define the least-altered value.

a step-leaching series as the nearly primary geochemical signal for the cap dolostones.

5.1.2. Interpretation of $\delta^{13}C$ and $\delta^{18}O$

As shown in Table 1 and Fig. 5a and b, carbon and oxygen isotope compositions of cap carbonates measured at 75 °C are slightly more enriched in ^{13}C and ^{18}O than those measured at 25 °C. This is mostly due to a large proportion of calcites in the samples, because (1) only calcite component in the samples releases CO_2 at 25 °C, whereas both dolomites and calcites would release CO_2 at 75 °C; (2) experimental calibrations suggest that oxygen isotope fractionations between dolomite and solution is smaller than between calcite and solution (Kim et al., 2007; Wang et al., 2013a), resulting in a more ^{18}O-enriched dolomite than coexisting calcite; (3) step-leaching experiments show that a large portion of calcites in samples has already been dissolved before the Mg/Ca ratios of the supernatants reach 0.8–0.9 (pure dolomite components). The more radiogenic $^{87}Sr/^{86}Sr$ values in the supernatants that have lower Mg/Ca ratios (<0.6 in steps S1 through S9/S10) indicate this calcite phase is secondary, mostly probably as a result of dedolomitization. Although this process could have reset $\delta^{18}O$ values and $^{87}Sr/^{86}Sr$ ratios of the calcitic components, the recrystallized calcites should have similar $\delta^{13}C$ values as original dolomite when water/rock ratio is high due to the low concentration of DIC in the fluid (Banner and Hanson, 1990; Veizer et al., 1999; Hoffman and Schrag, 2002; Kaufman and Knoll, 1995; Halverson et al., 2005). This is consistent with the lack of correlations between $\delta^{13}C$ and $\delta^{18}O$ (Fig. 5c), except for those samples that have $\delta^{18}O_{PDB}$ lower than −16‰ (probably indicating a higher water/rock ratio). We thus interpret most of our $\delta^{13}C$ results as the primary signal, showing a limited range around −2.2 to −2.5‰, but $\delta^{18}O$ values as the secondary. The low $\delta^{18}O_{PDB}$ values with a large range (−17 to −8‰) originated from meteoric/melt water interaction with original dolomite. This interpretation is consistent with previous studies which show many Neoproterozoic carbonates have altered O-isotope compositions, but still preserved the primary carbon isotopes (e.g. Kaufman and Knoll, 1995; Halverson et al., 2005). In particular, this negative $\delta^{13}C_{PDB}$ values from the Wushi DCC are consistent with the negative $\delta^{13}C$ composition of the Marinoan cap carbonates (Hoffman et al., 1998, 2007; Halverson et al., 2005, 2010; Raub, 2008; Macdonald et al., 2009; Johnston et al., 2012).

5.2. Least-altered Sr-isotope in cap dolostone of the Zhamoketi Formation

Different from samples of the Wushi DCC, Zhamoketi dolostones appear to have experienced more serious alterations, which could be related to two major tectonic events occurred in the Tianshan belt: Paleozoic closures of paleo-Tianshan oceans and Cenozoic deformation caused by India-Asia collision (Windley et al., 1990; Chen et al., 1999; Ge et al., 2012). Xiao et al. (2004) obtained very radiogenic $^{87}Sr/^{86}Sr$ ratios (0.71195–0.71364) from them using 1-step leaching experiments. These radiogenic $^{87}Sr/^{86}Sr$ ratios (ca. 0.711–0.713) are similar to our samples leached in step S1 through S13 (Table 2; Fig. 7a) after the surface adsorbates/evaporated salts were leached out in the first couple of steps and before five more steps were added (repetitions of step S13). But the Zhamoketi dolostones broadly show the similar patterns with the samples from the Wushi DCC during the progressive leaching, indicating that different phases in samples were effectively leached out, which is consistent with the step-leaching experiments on the Australia and Mongolia cap dolostones (Liu et al., 2013, 2014). Therefore, we also interpret the minimum $^{87}Sr/^{86}Sr$ from each leaching series as the least-altered values for the Zhamoketi samples for further discussion.

5.3. Origin of the Wushi cap carbonate and implications for the post-glacial ocean

Cap dolostones are typically transgressive sequence tracts following glaciations (Hoffman and Schrag, 2002; Nogueira et al., 2003; Font et al., 2006), supported by the widespread shallow-water features of low-angle cross-stratification, tube structure, giant-wave ripples, etc. (Aitken, 1991; James et al., 2001; Hoffman and Schrag, 2002; Corsetti and Grotzinger, 2005; Allen and Hoffman, 2005; Macdonald et al., 2009; Rose and Maloof, 2010). As the post-glacial sea level rises, the sedimentary base-level rises from low slope to platforms or continents (Hoffman et al., 2007; Hoffman, 2011), and dolostones grade upward into deep water limestone or shale, forming a complete "Cap-carbonate sequence" in lower slope (James et al., 2001; Hoffman and Schrag, 2002; Jiang et al., 2006). So, isotopic compositions of Sr and Mg from cap dolostones can provide a special perspective to understand the ocean environment in the transition of post-glaciation.

According to the least-altered values of $^{87}Sr/^{86}Sr$ and $\delta^{26}Mg_{DSM3}$, the Wushi cap dolostones can be categorized into two groups (Table 3 and Fig. 4c and d): Group A, samples from the lower subunit have average values of 0.7079 ± 0.0007 (1σ) for $^{87}Sr/^{86}Sr$ ratios and -1.46 ± 0.01‰ (1σ) for $\delta^{26}Mg_{DSM3}$, respectively; and Group B, samples from the upper subunit (~0.5 m above) have average values of 0.70687 ± 0.0003 (1σ) for $^{87}Sr/^{86}Sr$ and -1.60 ± 0.06‰ (1σ) for $\delta^{26}Mg_{DSM3}$. Obviously, the $^{87}Sr/^{86}Sr$ and $\delta^{26}Mg_{DSM3}$ values from the lower subunit are higher than those from the upper subunit, but still within the range of $^{87}Sr/^{86}Sr$ values from the contemporaneous limestone (Fig. 8; Halverson et al., 2007, 2010), and therefore could record the geochemical features of contemporary seawater.

Taken together with the distinct sedimentary transformation described in Section 3.1, the variations in $^{87}Sr/^{86}Sr$ and $\delta^{26}Mg$ values through the cap dolostone can be understood in a "plumeworld" framework, reflecting the various Sr and Mg input in an oscillatory water column during the post-Marinoan glaciation (Shields, 2005; Liu et al., 2014). In this model, the cap dolostones precipitated in the widespread glacial meltwater plume (Stage 2 in Liu et al., 2014) could record the elevated $^{87}Sr/^{86}Sr$ and $\delta^{26}Mg$ values sourced from continental silicate weathering (Tipper et al., 2006; Vance et al., 2009; Allègre et al., 2010), while in the subsequent overturned ocean stage (Stage 3 in Liu et al., 2014), the dolostones inherited the low $^{87}Sr/^{86}Sr$ and $\delta^{26}Mg$ ratios of the overturned seawater (Shields, 2005; Hurtgen et al., 2006; Liu et al., 2014). If this is the case, the lower and upper subunits of the cap dolostones in the Aksu-Wushi area may correspond to the glacial meltwater and overturn ocean deposition stages, respectively. Also, the near overlaps of $^{87}Sr/^{86}Sr$ ratios (Fig. 8) between the Zhamoketi cap dolostones (Quruqtagh) and the Group A samples from the Wushi DCC may suggest that the two cap dolostones formed in a same water plume, and this possibility will need to be addressed with more Sr and Mg isotopes from the Zhamoketi dolostones.

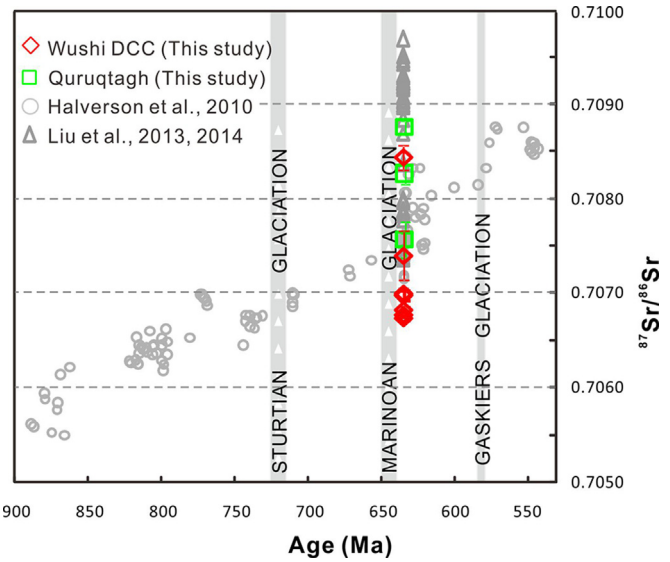

Fig. 8. Comparison of the new $^{87}Sr/^{86}Sr$ values from the cap dolostones of the Wushi DCC couplet (NW Tarim) and the Tereeken glaciation in the Quruqtagh area (NE Tarim) with the compilation of the strontium isotope data of seawater and glacial meltwater plume during the Neoproterozoic Era (from Halverson et al., 2010; Liu et al., 2013, 2014).

However, as shown in Fig. 8, there exist some discrepancies between our new $^{87}Sr/^{86}Sr$ values and those from the contemporaneous seawater and plume. First, the $^{87}Sr/^{86}Sr$ ratios (<0.7070) from the upper subunit dolostones of Wushi DCC are slightly lower than the values obtained from the Marinoan limestone (Halverson et al., 2007, 2010). Second, the $^{87}Sr/^{86}Sr$ values of the glacial meltwater plume in Tarim (Wushi and Quruqtagh) are lower, while $\delta^{26}Mg$ are higher than the plume where the cap dolostones precipitated in Australia and Mongolia (i.e., the Nuccaleena Formation in Australia and the Ol Formation in Mongolia; Liu et al., 2013, 2014). These discrepancies can be explained in the following alternative ways: (1) the Wushi DCC samples could be explained, based on the slightly lower $^{87}Sr/^{86}Sr$ ratios, as Sturtian cap dolostone, but this interpretation is inconsistent with our field observations and age-constraints described in Section 3.3; (2) the lower $^{87}Sr/^{86}Sr$ ratio could represent the earliest precipitation after glaciation, when the sea-floor volcanism could have supplied both mantle-like $^{87}Sr/^{86}Sr$ and abundant CO_2 released to the atmosphere which has been proposed as a driving force for triggering the deglaciation (e.g. Shields, 2005; Hoffman, 2011), but this hydrothermal input should have little effect on $\delta^{26}Mg$ elevation in seawater (e.g. Tipper et al., 2006; Vance et al., 2009; Allègre et al., 2010); (3) the dolostone in Tarim was formed close to ridges with the continuous influence of hydrothermal fluid, which can explain the slightly lower $^{87}Sr/^{86}Sr$ ratios and higher $\delta^{26}Mg$ values than the sections in Austria and Mongolia (Liu et al., 2013, 2014), due to higher precipitation temperatures (Wang et al., 2013b; Saenger and Wang, 2014; Li et al., 2015); and (4) the cap dolostone in Tarim was formed from a water body that was isolated from the ocean where dolostones

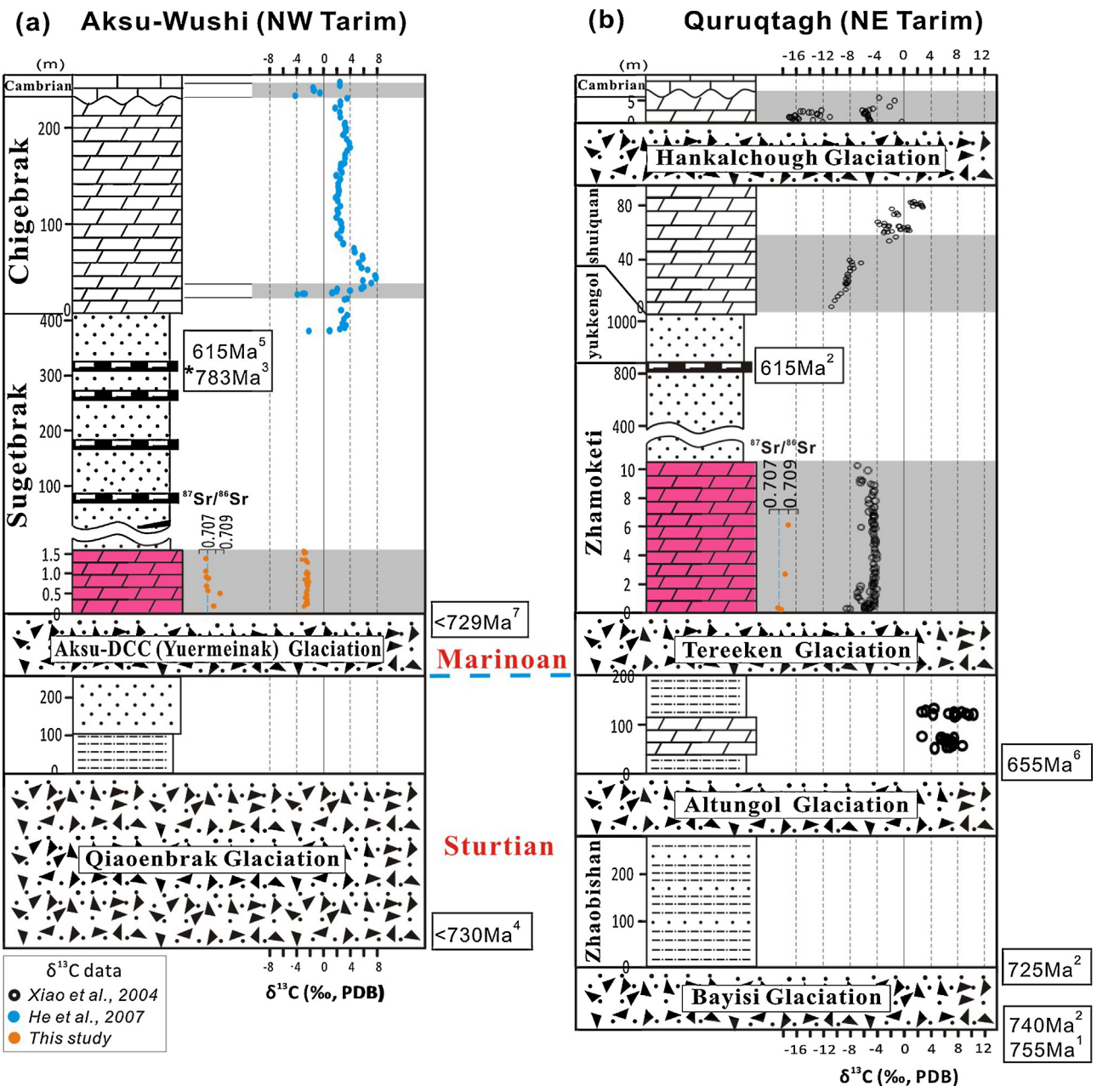

Fig. 9. Stratigraphic and glacial correlations between the Aksu-Wushi area (a) and the Quruqtagh area of eastern Tianshan (b) in northern Tarim (see Section 5.4). The available ages are also shown (data from 1, Xu et al., 2005;2, Xu et al., 2009;3, Zhang et al., 2012;4, Wen et al., 2013;5, Xu et al., 2013;6, He et al., 2014a;7, He et al., 2014b), and the ages with (*) are considered as dating inherited/xenocryst zircons. Lithofacies legend and abbreviations are the same as in Fig. 2. Note variable thickness scales.

from Australia and Mongolia were formed, having input of Sr and Mg from different sources (Tipper et al., 2006; Vance et al., 2009; Allègre et al., 2010). Such discrepancy may highlight additional complications in interpreting $^{87}Sr/^{86}Sr$ ratios of the Neoproterozoic carbonates: inter-sample variability and fine-scale diachroneity of the studied carbonate sections allow for the possibility, and perhaps even likelihood, that even the lowest measured ratios may overestimate the seawater ratio from a given epoch. All the possibilities shall be investigated in future studies of the area.

5.4. New stratigraphic correlation between NW Tarim and Quruqtagh area in NE Tarim

Putting together the new geochemical data with the stratigraphic framework in the Aksu-Wushi region (Section 3.3), a new stratigraphic correlation between NW Tarim and the typical Quruqtagh area in NE Tarim for the late Neoproterozoic successions is given in Fig. 9. In the new correlations, the Aksu (Yuermeinak) diamictite and the Wushi DCC couplet represent the Marinoan glaciation and the aftermath cap carbonate in the Cryogenian-Ediacaran transition, filling the depositional gap between the underlying diamictites and the overlying strata in previous stratigraphic successions (e.g. Gao et al., 1985; XBGMR, 1993; Zhu and Wang, 2011). Their equivalents, Tereeken glaciation and atop cap dolostone (Zhamoketi) from Quruqtagh, have been correlated to the Marinoan glaciations based on sedimentary features and chemostratigraphic patterns of the cap carbonates (Xiao et al., 2004), and further reinforced by the recent zircon U–Pb ages from volcanic layers below and above the Zhamoketi Formation (Xu et al., 2009; He et al., 2014a). Also, as discussed above, the new $^{87}Sr/^{86}Sr$

ratios suggest that the lower subunit dolostone of the Wushi DCC and the Zhamoketi cap dolostones probably share a same post-glacial "plumewater" that was isolated from the ocean where other cap dolostones formed.

If so, our new C-isotope data and the data from the uppermost Sugetbrak, Chigebrak Formations and the Early Cambrian limestone (He et al., 2007), three negative $\delta^{13}C$ anomalies for the Aksu-Wushi area (Fig. 9a) could be correlated with those from the Quruqtagh sequences (Fig. 9b; Xiao et al., 2004; Shen et al., 2008), corresponding to the last three negative $\delta^{13}C$ anomalies during the late Neoproterozoic: Marinoan glaciations, mid-Ediacaran Wonoka-Shuram, and Precambrian-Cambrian boundary, respectively (Halverson et al., 2005, 2010; Le Guerroué, 2010). Accordingly, an older, probably Neoproterozoic Sturtian-age glaciation would correlate with the underlying Qiaoenbrak and Bayisi/Altungol Formations (Fig. 9), a hypothesis which needs further tests with precise geochronological data in the future.

6. Conclusions

We have conducted detailed field investigations in the Aksu-Wushi area of the northwestern margin of Tarim Craton. New Cryogenian diamictite and a diamictite and cap carbonate (DCC) couplet are discovered at Aksu and Wushi sections, respectively. The Aksu diamictite displays glaciogenic features such as striations on clasts, whereas the DCC couplet hosts diamictite and overlying cap dolostone. The regional stratigraphy, sedimentological characteristics, paleontological markers, as well as available age constraints indicate that the Aksu diamictite-Wushi DCC are of Marinoan age. High-resolution C isotope records of the cap dolostone from the Wushi DCC show carbon isotope compositions similar to those of other Marionan cap carbonates. The least-altered Sr-, Mg-isotopes were extracted from the Wushi DCC and the Tereeken cap dolostone, i.e., the Zhamoketi Formation from northeastern Tarim, using a recently developed, incremental step-leaching method. These data provide additional new insights into the paleoenvironmental conditions of post-glacial oceans.

Acknowledgments

We would like to thank Brad Erkkila and Ross Anderson for technical help to conduct C–O isotopic and Sr isotopic analysis respectively, Shipeng Wang, Tao Xu, and Huadong Ma for field assistance, and Paul F. Hoffman for providing constructive suggestions. Galen P. Halverson and Shuhai Xiao kindly made the compiled Sr isotopic data and Quruqtagh samples available to us, respectively, for which we express our thanks. We also thank two anonymous reviewers for their constructive comments to improve this manuscript. This research was funded by National Natural Science Foundation of China (41274071, 41230208) and Yale University. B. Wen is funded by a state scholarship grant from China Scholarship Council (CSC) and a graduate research fellowship (No. 201501B027) from Nanjing University.

References

Aitken, J.D., 1991. The Ice Brook Formation and Post-Rapitan, Late Proterozoic Glaciation, Mackenzie Mountains, Northwest Territories: Geological Survey of Canada Bulletin 404, 43 pp.

Allègre, C.J., Louvat, P., Gaillardet, J., Meynadier, L., Rad, S., Capmas, F., 2010. The fundamental role of island arc weathering in the oceanic Sr isotope budget. Earth Planet. Sci. Lett. 292, 51–56.

Allen, P.A., Hoffman, P.F., 2005. Extreme winds and waves in the aftermath of a Neoproterozoic glaciation. Nature 433, 123–127.

Bailey, T.R., McArthur, J.M., Prince, H., Thirlwall, M.F., 2000. Dissolution methods for strontium isotope stratigraphy: whole rock analysis. Chem. Geol. 167, 313–319.

Banner, J.L., Hanson, G.N., 1990. Calculation of simultaneous isotopic and trace element variations during water-rock interaction with applications to carbonate diagenesis. Geochem. Cosmochim. Acta 54, 3123–3137.

Calver, C.R., Crowley, J.L., Wingate, M.T.D., Evans, D.A.D., Raub, T.D., Schmitz, M.D., 2013. Globally synchronous Marinoan deglaciation indicated by U–Pb geochronology of the Cottons Breccia, Tasmania, Australia. Geology 41, 1127–1130.

Carroll, A.R., Graham, S.A., Chang, E.Z., McKnight, C., 2001. Sinian through Permian tectonostratigraphic evolution of the northwestern Tarim basin, China. Geol. Soc. Am. Mem. 194, 47–69.

Chen, C.M., Lu, H.F., Jia, D., Cai, D.S., Wu, S.M., 1999. Closing history of the southern Tianshan oceanic basin, western China: an oblique collisional orogeny. Tectonophysics 302, 23–40.

Chen, Y., Xu, B., Zhan, S., Li, Y.A., 2004. First mid-Neoproterozoic paleomagnetic results from the Tarim Basin (NW China) and their geodynamic implications. Precambrian Res. 133, 271–281.

Condon, D.J., Bowring, S.A., 2011. The geological record of Neoproterozoic glaciations. Geol. Soc. Lond. Mem. 36, 135–149.

Condon, D., Zhu, M.Y., Bowring, S., Wang, W., Yang, A.H., Jin, Y.G., 2005. U–Pb ages from the Neoproterozoic Doushantuo formation, China. Science 308, 95–98.

Corsetti, F.A., Grotzinger, J.P., 2005. Origin and significance of tube structures in Neoproterozoic post-glacial cap carbonates: example from Noonday Dolomite, Death Valley, United States. Palaios 20, 348–362.

Corsetti, F.A., Kaufman, A.J., 2003. Stratigraphic investigations of carbon isotope anomalies and Neoproterozoic ice ages in Death Valley, California. Geol. Soc. Am. Bull. 115, 916–932.

Ding, H.F., Ma, D.S., Yao, C.Y., Shu, L.S., 2009. Sedimentary environment of Ediacaran glacigenic diamictite in Guozigou of Xinjiang, China. Chin. Sci. Bull. 54, 3283–3294.

Evans, D.A.D., 2000. Stratigraphic, geochronological, and paleomagnetic constraints upon the Neoproterozoic climatic paradox. Am. J. Sci. 300, 347–433.

Evans, D.A.D., Raub, T.D., 2011. Neoproterozoic glacial palaeolatitudes: a global update. Geol. Soc. Lond. Mem. 36, 93–112.

Font, E., Nédélec, A., Trindade, R.I.F., Macouin, M., Charrière, A., 2006. Chemostratigraphy of the Neoproterozoic Mirassold'Oeste cap dolostones (Mato Grosso, Brazil): an alternative model for Marinoan cap dolostone formation. Earth Planet. Sci. Lett. 250, 89–103.

Font, E., Trindade, R.I.F., Nédélec, A., 2005. Detrital remanent magnetization in haematite-bearing Neoproterozoic Puga cap dolostone, Amazon craton: a rock magnetic and SEM study. Geophys. J. Int. 163, 491–500.

Galy, A., Yoffe, O., Janney, P.E., Williams, R.W., Cloquet, C., Alard, O., Halicz, L., Wadhwa, M., Hutcheon, I.D., Ramon, E., Carignan, J., 2003. Magnesium isotope heterogeneity of the isotopic standard SRM980 and new reference materials for magnesium-isotope-ratio measurements. J. Anal. At. Spectrom. 18, 1352–1356.

Gao, G.Q., 1990. Geochemical and isotopic constraints on the diagenetic history of a massive stratal, late Cambrian (Royer) dolomite, Lower Arbuckle Group, Slick Hills, SW Oklahoma, USA. Geochem. Cosmochim. Acta 54, 1979–1989.

Gao, Z.J., Qian, J.X., 1985. Sinian glacial deposits in Xinjiang, northwestern China. Precambrian Res. 29, 143–147.

Gao, Z.J., Wang, W.Y., Peng, C.W., Li, Y.A., Xiao, B., Urumqi (in Chinese with English abstract) 1985. The Sinian System of Xinjiang. Xinjiang People's Publishing House.

Gao, Z., Zhu, S., 1984. Precambrian Geology in Xinjiang, China. Xinjiang People's Publishing House, Urumqi, China.

Ge, R.F., Zhu, W.B., Wilde, S.A., He, J.W., 2014. Zircon U–Pb–Lu–Hf–O isotopic evidence for ≥3.5 Ga crustal growth, reworking and differentiation in the northern Tarim Craton. Precambrian Res. 249, 115–128.

Ge, R.F., Zhu, W.B., Wu, H.L., Zheng, B.H., Zhu, X.Q., He, J.W., 2012. The Paleozoic northern margin of the Tarim Craton: passive or active? Lithos 142–143, 1–15.

Gradstein, F.M., Ogg, J.G., Smith, A.G., Bleeker, W., Lourens, L.J., 2004. A new Geologic Time Scale, with special reference to Precambrian and Neogene. Episodes 27, 83–100.

Halverson, G.P., Dudás, F.ő., Maloof, A.C., Bowring, S.A., 2007. Evolution of the $^{87}Sr/^{86}Sr$ composition of Neoproterozoic seawater. Palaeogeogr. Palaeoclimatol. Palaeoecol. 256, 103–129.

Halverson, G.P., Hoffman, P.F., Schrag, D.P., Maloof, A.C., Rice, A.H., 2005. Toward a Neoproterozoic composite carbon-isotope record. Geol. Soc. Am. Bull. 117, 1181–1207.

Halverson, G.P., Hurtgen, M.T., Porter, S.M., Collins, A.S., 2010. Neoproterozoic-Cambrian biogeochemical evolution. Dev. Precambrian Geol. 16, 351–366.

He, X.B., Xu, B., Yuan, Z.Y., 2007. C-isotope composition and correlation of the Upper Neoproterozoic in Keping area, Xinjiang. Chin. Sci. Bull. 52, 504–511.

He, J.W., Zhu, W.B., Ge, R.F., 2014a. New age constraints on Neoproterozoic diamicites in Kuruktag, NW China and Precambrian crustal evolution of the Tarim Craton. Precambrian Res. 241, 44–60.

He, J.W., Zhu, W.B., Ge, R.F., Zheng, B.H., Wu, H.L., 2014b. Detrital zircon U–Pb ages and Hf isotopes of Neoproterozoic strata in the Aksu area, northwestern Tarim Craton: implications for supercontinent reconstruction and crustal evolution. Precambrian Res. 254, 194–209.

Hoffman, P.F., 2011. Strange bedfellows: glacial diamictite and cap carbonate from the Marinoan (635 Ma) glaciation in Namibia. Sedimentology 58, 57–119.

Hoffman, P.F., Halverson, G.P., Domack, E.W., Husson, J.M., Higgins, J.A., Schrag, D.P., 2007. Are basal Ediacaran (635 Ma) post-glacial "cap dolostones" diachronous? Earth Planet. Sci. Lett. 258, 114–131.

Hoffman, P.F., Kaufman, A.J., Halverson, G.P., Schrag, D.P., 1998. A Neoproterozoic snowball Earth. Science 281, 1342–1346.

Hoffman, P.F., Li, Z.X., 2009. Palaeogeogr. Palaeoclimatol. Palaeoecol. 277, 158–172.
Hoffman, P.F., Schrag, D.P., 2002. The snowball Earth hypothesis: testing the limits of global change. Terra Nova 14, 129–155.
Hoffmann, K.H., Condon, D.J., Bowring, S.A., Crowley, J.L., 2004. U–Pb zircon date from the Neoproterozoic Ghaub Formation, Namibia: constraints on Marinoan glaciation. Geology 32, 817–820.
Hurtgen, M.T., Halverson, G.P., Arthur, M., Hoffman, P.F., 2006. Sulfur cycling in the aftermath of a 635-Ma snowball glaciation: evidence for a syn-glacial sulfidic deep ocean. Planet. Sci. Lett. 245, 551–570.
James, N.P., Narbonne, G.M., Kyser, T.K., 2001. Late Neoproterozoic cap carbonates: Mackenzie Mountains, northwestern Canada: precipitation and global glacial meltdown. Can. J. Earth Sci. 38, 1229–1262.
Jiang, G.Q., Kennedy, M.J., Christie-Blick, N., Wu, H.C., Zhang, S.H., 2006. Stratigraphy, sedimentary structures, and textures of the late Neoproterozoic Doushantuo cap carbonate in South China. J. Sediment. Res. 76, 978–995.
Johnston, D.T., Macdonald, F.A., Gill, B.C., Hoffman, P.F., Schrag, D.P., 2012. Uncovering the Neoproterozoic carbon cycle. Nature 483, 320–323.
Kaufman, A.J., Knoll, A.H., 1995. Neoproterozoic variations in the C-isotopic composition of seawater: stratigraphic and biogeochemical implications. Precambrian Res. 73, 27–49.
Kaufman, A.J., Knoll, A.H., Narbonne, G.M., 1997. Isotopes, ice ages, and terminal Proterozoic earth history. Proc. Natl. Acad. Sci. USA 94, 6600–6605.
Kennedy, M.J., Runnegar, B., Prave, A.R., Hoffmann, K.H., Arthur, M.A., 1998. Two or four Neoproterozoic glaciations? Geology 26, 1059–1063.
Kim, S., O'Neil, J., Hillaire-Marcel, C., Mucci, A., 2007. Oxygen isotope fractionation between synthetic aragonite and water: influence of temperature and Mg^{2+} concentration. Geochim. Cosmochim. Acta 71, 4704–4715.
Knoll, A.H., 2014. Paleobiological perspectives on early eukaryotic evolution. Cold Spring Harb. Perspect. Biol. 6, 1–14.
Knoll, A.H., Walter, M.R., 1992. Latest Proterozoic stratigraphy and Earth history. Nature 356, 673–677.
Knoll, A.H., Walter, M.R., Narbonne, G.M., Christie-Blick, N., 2004. A New Period for the Geologic Time Scale. Science 305, 621–622.
Le Guerroué, E., 2010. Duration and synchroneity of the largest negative carbon isotope excursion on Earth: the Shuram/Wonoka anomaly. C. R. Geosci. 342, 204–214.
Li, W., Beard, B.L., Li, C., Xu, H., Johnson, C.M., 2015. Experimental calibration of Mg isotopefractionation between dolomite and aqueous solution and its geological implications. Geochim. Cosmochim. Acta, http://dx.doi.org/10.1016/j.gca.2015.02.024.
Li, Z.X., Bogdanova, S.V., Collins, A.S., Davidson, A., De Waele, B., Ernst, R.E., Fitzsimons, I.C.W., Fuck, R.A., Gladkochub, D.P., Jacobs, J., Karlstrom, K.E., Lu, S., Natapov, L.M., Pease, V., Pisarevsky, S.A., Thrane, K., Vernikovsky, V., 2008. Assembly, configuration, and break-up history of Rodinia: a synthesis. Precambrian Res. 160, 179–210.
Liou, J.G., Graham, S.A., Maruyama, S., Wang, X., Xiao, X., Carroll, A.R., Chu, J., Feng, Y., Hendrix, M.S., Liang, Y.H., McKnight, C.L., Tang, Y., Wang, Z.X., Zhao, M., Zhu, B., 1989. Proterozoic blueschist belt in western China: best documented Precambrian blueschists in the world. Geology 17, 1127–1131.
Liou, J.G., Graham, S.A., Maruyama, S., Zhang, R.Y., 1996. Characteristics and tectonic significance of the Late Proterozoic Aksu blueschists and diabasic dikes, northwest Xinjiang, China. Int. Geol. Rev. 38, 228–244.
Liu, C., 152 pp. 2014. Sr and Mg Isotope Geochemistry of Marinoan Cap Carbonates, Ph.D Dissertation. Yale University.
Liu, C., Wang, Z.R., Raub, T.D., 2013. Geochemical constraints on the origin of Marinoan cap dolostone from Nuccaleena Formation, South Australia. Chem. Geol. 351, 95–104.
Liu, C., Wang, Z.R., Raub, T.D., Macdonald, F.A., Evans, D.A.D., 2014. Neoproterozoic cap-dolostone deposition in stratified glacial meltwater plume. Earth Planet. Sci. Lett. 404, 22–32.
Long, X.P., Sun, M., Yuan, C., Krőner, A., Hu, A.q., 2012. Zircon REE patterns and geochemical characteristics of Paleoproterozoic anatectic granite in the northern Tarim Craton, NW China: implications for the reconstruction of the Columbia supercontinent. Precambrian Res. 222–223, 474–487.
Long, X.P., Yuan, C., Sun, M., Zhao, G.C., Xiao, W.J., Wang, Y.J., Yang, Y.C., Hu, A.q., 2010. Archean crustal evolution of the northern Tarim Craton, NW China: zircon U–Pb and Hf isotopic constraints. Precambrian Res. 180, 272–284.
Lu, S.N., Li, H.K., Zhang, C.L., Niu, G.H., 2008. Geological and geochronological evidence for the Precambrian evolution of the Tarim Craton and surrounding continental fragments. Precambrian Res. 160, 94–107.
Macdonald, F.A., Jones, D.S., Schrag, D.P., 2009. Stratigraphic and tectonic implications of a newly discovered glacial diamictite-cap carbonate couplet in southwestern Mongolia. Geology 37, 123–126.
Nakajima, T., Maruyama, S., Uchiumi, S., Liou, J.G., Wang, X., Xiao, X., Graham, S.A., 1990. Evidence for late Proterozoic subduction from 700-Myr-old blueschists in China. Nature 346, 262–265.
Nogueira, A.C.R., Riccomini, C., Sial, A.N., Moura, C.A.V., Fairchild, T.R., 2003. Soft-sediment deformation at the base of the Neoproterozoic Puga cap carbonate (southwestern Amazon Craton, Brazil): confirmation of rapid icehouse to greenhouse transition in snowball Earth. Geology 31, 613–616.
Norin, E., 1937. Reports from the Scientific Expedition to the Northwestern Provinces of China under the Leadership of Dr. Sven Hedin, III. Geology, 1. Geology of Western Quruqtagh, Eastern Tien-Shan. Bokförlags Aktiebolaget Thule, Stockholm, 194 pp.
Raub, T.D., 2008. Prolonged Deglaciation of Snowball Earth, Dissertation. Yale University, 296 pp.
Raub, T.D., Evans, D.A.D., Smirnov, A.V., 2007. Siliciclastic prelude to Elatina-Nuccaleena deglaciation: lithostratigraphy and rock magnetism of the base of the Ediacaran system. Geol. Soc. Lond. 286, 53–76.
Rose, C.V., Maloof, A.C., 2010. Testing models for post-glacial 'cap dolostone' deposition: Nuccaleena Formation, South Australia. Earth Planet. Sci. Lett. 296, 165–180.
Saenger, C., Wang, Z.R., 2014. Magnesium isotope fractionation in biogenic and abiogenic carbonates: implications for paleoenvironmental proxies. Quatern. Sci. Rev. 90, 1–21.
Shen, B., Xiao, S.H., Kaufman, A.J., Bao, H.M., Zhou, C.M., Wang, H.F., 2008. Stratification and mixing of a post-glacial Neoproterozoic ocean: evidence from carbon and sulfur isotopes in a cap dolostone from northwest China. Earth Planet. Sci. Lett. 265, 209–228.
Shields, G.A., 2005. Neoproterozoic cap carbonates: a critical appraisal of existing models and the plumeworld hypothesis. Terra Nova 17, 299–310.
Stratigraphy Committee of China, Beijing (in Chinese) 2001. China Stratigraphic Guide and Exposition on China Stratigraphic Guide, (revised edition). Geology Publishing House.
Tipper, E.T., Galy, A., Gaillardet, J., Bickle, M.J., Elderfield, H., Carder, E.A., 2006. The magnesium isotope budget of the modern ocean: constraints from riverine magnesium isotope ratios. Planet. Sci. Lett. 250, 241–253.
Torsvik, T.H., 2003. The Rodinia jigsaw puzzle. Science 300, 1379–1381.
Turner, S.A., 2010. Sedimentary record of Late Neoproterozoic rifting in the NW Tarim Basin, China. Precambrian Res. 181, 85–96.
Turner, S.A., Cosgrove, J.W., Liu, J.G., 2010. Controls on lateral structural variability along the Keping Shan Thrust Belt, SW Tien Shan Foreland, China. Geol. Soc. Lond. 348, 71–85.
Vance, D., Teagle, D.A.H., Foster, G., 2009. Variable Quaternary chemical weathering fluxes and imbalances in marine geochemical budgets. Nature 458, 493–496.
Veizer, J., Ala, D., Azmy, K., Bruckschen, P., Buhl, D., Bruhn, F., Carden, G.A.F., Diener, A., Ebneth, S., Godderis, Y., Jasper, T., Korte, C., Pawellek, F., Podlaha, O.G., Strauss, H., 1999. $^{87}Sr/^{86}Sr$, $\delta^{13}C$ and $\delta^{18}O$ evolution of Phanerozoic seawater. Chem. Geol. 161, 59–88.
Wang, B., 2006. Paleozoic Geodynamic Evolution of Yili Block in West Chinese Tianshan, Ph.D Dissertation. Nanjing University, 153 pp. (in Chinese with English abstract).
Wang, Z.R., Gaetani, G., Liu, C., Cohen, A., 2013a. Oxygen isotope fractionation between aragonite and seawater: developing a novel kinetic oxygen isotope fractionation model. Geochim. Cosmochim. Acta 117, 232–251.
Wang, Z.R., Hu, P., Gaetani, G., Liu, C., Saenger, C., Cohen, A., Hart, S., 2013b. Experimental calibration of Mg isotope fractionation between aragonite and seawater. Geochem. Cosmochim. Acta 102, 113–123.
Wen, B., 2014. Rock magnetic study of Neoproterozoic cap carbonates. IRM Q. 24, 2–3.
Wen, B., Li, Y.X., Zhu, W.B., 2013. Paleomagnetism of the Neoproterozoic diamictites of the Qiaoenbrak formation in the Aksu area, NW China: constraints on the paleogeographic position of the Tarim Block. Precambrian Res. 226, 75–90.
Windley, B.F., Allen, M.B., Zhang, C., Zhao, Z.Y., Wang, G.R., 1990. Paleozoic accretion and Cenozoic redeformation of the Chinese Tien Shan Range, central Asia. Geology 18, 128–131.
Xinjiang Bureau of Geology and Mineralogy Resources (XBGMR), 1993. Regional Geology of Xinjiang Uygur Autonomy Region. Geology Publishing House, Beijing (in Chinese with English abstract).
Xiao, S.H., Bao, H.M., Wang, H.F., Kaufman, A.J., Zhou, C.M., Li, G.X., Yuan, X.L., Ling, H.F., 2004. The Neoproterozoic Quruqtagh Group in eastern Chinese Tianshan: evidence for a post-Marinoan glaciations. Precambrian Res. 130, 1–26.
Xu, B., Jian, P., Zheng, H.F., Zou, H.B., Zhang, L.F., Liu, D.Y., 2005. U–Pb zircon geochronology and geochemistry of Neoproterozoic volcanic rocks in the Tarim Block of northwest China: implications for the breakup of Rodinia supercontinent and Neoproterozoic glaciations. Precambrian Res. 136, 107–123.
Xu, B., Xiao, S.H., Zou, H.B., Chen, Y., Li, Z.X., Song, B., Liu, D.Y., Zhou, C.M., Yuan, X.L., 2009. SHRIMP zircon U–Pb age constraints on Neoproterozoic Quruqtagh-diamictites in NW China. Precambrian Res. 168, 247–258.
Xu, B., Zou, H.B., Chen, Y., He, J.Y., Wang, Y., 2013. The Sugetbrak basalts from northwestern Tarim Block of northwest China: geochronology, geochemistry and implications for Rodinia breakup and ice age in the Late Neoproterozoic. Precambrian Res. 236, 214–226.
Yao, J.X., Xiao, S.H., Yin, L.M., Li, G.X., Yuan, X.L., 2005. Basal Cambrian Microfossils from the Yurtus and Xishanbulaq formations (Tarim, North-West China): systemic revision and biostratigraphic correlation of Micrhystridium-like acritarchs. Paleontology 48, 687–708.
Zhan, S., Chen, Y., Xu, B., Wang, B., Faure, M., 2007. Late Neoproterozoic paleomagnetic results from the Sugetbrak Formation of the Aksu area, Tarim basin (NW China) and their implications to paleogeographic reconstructions and the snowball Earth hypothesis. Precambrian Res. 154, 143–158.
Zhang, S.H., Jiang, G.Q., Han, Y.G., 2008. The age of the Nantuo Formation and Nantuo glaciation in South China. Terra Nova 20, 289–294.
Zhang, Z.C., Kang, J., Kusky, T., Santosh, M., Huang, H., Zhang, D.Y., Zhu, J., 2012. Geochronology, geochemistry and petrogenesis of Neoproterozoic basalts from Sugetbrak, northwest Tarim block, China: implications for the onset of Rodinia supercontinent breakup. Precambrian Res. 220–221, 158–176.
Zhang, C.L., Li, Z.X., Li, X.H., Ye, H.M., 2009. Neoproterozoic mafic dyke swarms at the northern margin of the Tarim Block, NW China: age, geochemistry, petrogenesis and tectonic implications. J. Asian Earth Sci. 35, 167–179.

Zhao, G.C., Cawood, P.A., 2012. Precambrian geology of China. Precambrian Res. 222–223, 13–54.
Zhao, G.C., Guo, J.H., 2012. Precambrian geology of China: preface. Precambrian Res. 222–223, 1–12.
Zhao, G.C., Wilde, S.A., Cawood, P.A., Sun, M., 2002. SHRIMP U–Pb zircon ages of the Fuping complex: implications for late Archean to Paleoproterozoic accretion and assembly of the North China Craton. Am. J. Sci. 302, 191–226.
Zhu, M.Y., Wang, H.F., 2011. Neoproterozoic galciogenic diamictites of the Tarim Block, NW China. Geol. Soc. Lond. Mem. 36, 367–378.
Zhu, W.B., Zheng, B.H., Shu, L.S., Ma, D.S., Wu, H.L., Li, Y.X., Huang, W.T., Yu, J.J., 2011. Neoproterozoic tectonic evolution of the Precambrian Aksublueschistterrane, northwestern Tarim, China: insights from LA-ICP-MS zircon U–Pb ages and geochemical data. Precambrian Res. 185, 215–230.